Experimental and Theoretical Investigation of Monolayer Phase Separation on Noble Metal Nanoparticles

---

A Thesis

Presented to

the faculty of the School of Engineering and Applied Science

University of Virginia

---

in partial fulfillment
of the requirements for the degree

Doctor of Philosophy

by

Steven N. Merz

December 2018

APPROVAL SHEET

This Thesis
is submitted in partial fulfillment of the requirements
for the degree of
Doctor of Philosophy

Author Signature: _____

This Thesis has been read and approved by the examining committee:

Advisor: David Green

Committee Member: Kateri DuBay

Committee Member: Sergei Egorov

Committee Member: Joshua Choi

Committee Member: Gary Koenig

Committee Member: _____

Accepted for the School of Engineering and Applied Science:

Craig H. Benson, School of Engineering and Applied Science

December 2018

Abstract

Monolayer protected nanoparticles (MNPs) have a wide variety of applications from catalysis and photonics to biosensing and drug delivery. However, characterization of ultrasmall MNPs (< 10nm) has proven difficult with traditional experimental techniques, making the synthesis and design of these ultrasmall MNPs challenging. Our work looks to develop simple and robust characterization methods using both experimental and computational techniques.

Experimentally we use Transmission Electron Microscopy (TEM) to assess nanoparticle shape and size and Matrix-Assisted Laser Desorption and Ionization (MALDI) to assess the degree of order present in nanoparticle monolayers. In addition, we model the systems using both Self-Consistent Field Theory (SCFT) and atomistic simulations to model these nanoparticle monolayers. We are then able to calculate predicted MALDI spectrum from these simulations which allows us to directly compare theory and experiment.

We validate this method with our first paper looking at a monolayer with only isotopic differences (dodecanethiol (DDT) and deuterated dodecanethiol [D25]DDT) as our control monolayer with a physically mismatched monolayer (DDT and butanethiol (BT)) that should show signs of phase separation. Our work looking at these two types of monolayers shows strong matches confirmed our hypothesized morphologies which gives strong credence to our technique.

We use our method to explore the dynamics of phase separation in a variety multi-ligand nanoparticle monolayers. This method is first used to examine how various degrees of physical mismatch between ligands effect nanoprticle monolayer phase separation, giving us a detailed look at how small changes in chain length mismatch between ligands can lead to a range of differing striped monolayers. We then expand our method to look at patchy and Janus-like phases by examining multi-ligand nanoparticle monolayers with chemical mismatch. The modelling of chemically mismatched monolayers required the use of more accurate atomistic simulations with advanced Monte Carlo sampling. These more advanced computational techniques allows for an accurate modelling of Janus-like monolayer phase separation. The CBMC atomistic simulation is also shown to be even more versatile by de novo predicting monolayer phase separation in monolayers with a variety of physical and chemical mismatches which gives rise to the possibility of computational design of multi-ligand nanoparticle monolayers for applications in drug delivery, biosensing, and photonics.

Acknowledgements

I would like to acknowledge the help and support I received from my family, friends and colleagues during my time completing my PhD. First my parents Gary and Terri Merz for the continued love and support. I would also like to thank Dr. Zachary Farrell for his key role in developing the experimental techniques used within this work. I would also like to acknowledge Dr. David Green for his valuable advice and guidance throughout this process. A large thanks to Dr. Kateri DuBay, who has been instrumental in providing guidance and mentoring on computational techniques which underly a large portion of this work. I would like to also thank Dr. Sergei Egorov for his advice and guidance, especially on the use of self-consistent field theory.

I would also like to acknowledge funding I received from the ACS-PRF grant No. 53934-ND6, which was used in funding the work presented below.

Contents

List of Figures

Chapter 1

Introduction

Nanoparticles have found a wide array of uses from composites and colloids to drug delivery and biological imaging [1]. One of the unique aspects of nanoparticles are their high surface area to volume ratio which allows surface effects to dominate. This results in unique effects not seen in bulk materials. These effects include surface plasmon resonance, surfactant properties, and unique self-assembled structures. With nanoparticle surfaces playing such a large role in their overall properties, tuning this interfacial area on the nanoparticle is crucial to controlling its properties.

One of the most common ways of modifying nanoparticle properties is by modifying the nanoparticle surface. There are several techniques to achieve this including core-shell synthesis [2], liposome encapsulation [3], as well as the addition of a ligand monolayer [4]. In our work, we focus on modifying the nanoparticle surface with a ligand monolayer as this method allows for a wide array of differing ligand types and has a straightforward way of attaching useful molecules via click chemistry [5,6]. Another advantage of monolayer protected nanoparticles (MPN's) is the ease of adding additional functionality by using multiple ligand types. These multifunctional nanoparticles are especially useful in drug delivery applications, where one wishes to have a ligand with functional groups suited for targeted delivery along with other ligand types used for carrying the drug [7, 8].

One crucial aspect of multi-ligand monolayers is monolayer phase separation. As two different ligand types adsorb to the surface of the nanoparticle, they will tend to separate into varying phases depending on the physical and chemical characteristics of the ligands (see Figure 1.1). Previous work by other groups has shown that the type of monolayer phase separation on a MPN can have a drastic effect on its properties as a drug delivery agent [9–12], as a catalyst [13,14], and allows unique self-assembled structures to form [15–18]. Thus, controlling this phase separation is a crucial step in tuning MPN properties.

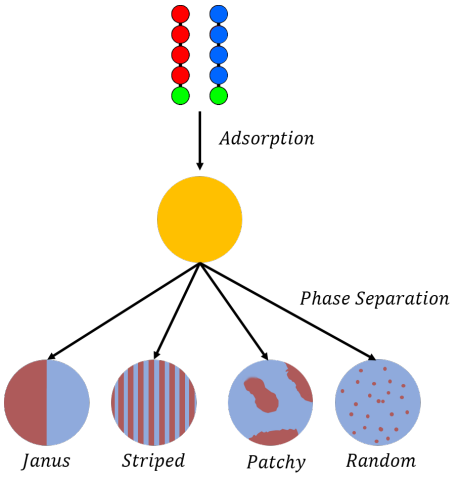

Figure 1.1: Diagram of phase separation in multi-ligand nanoparticle monolayers. Here we see that two different ligand types (red and blue) adsorb onto the monolayer and subsequently undergo phase separation to self-assemble into one of several different types of monolayer structures.

Our work looks to find the underlying factors behind this phase separation by studying monolayer phase separation under a variety of conditions using both experimental and theoretical techniques. In doing so we hope to develop a systematic method for engineering phase separation from a set of design principles based on the chemical and physical differences between ligands in multi-ligand monolayer. These design principles will allow others to predict and design the spatial patterning of these nanoparticle monolayers and thereby control the monolayer protected nanoparticle properties (see Figure 1.2). These design principles can then be applied to facilitate better design of MPN based catalysts, drug delivery, and bio-imaging devices.

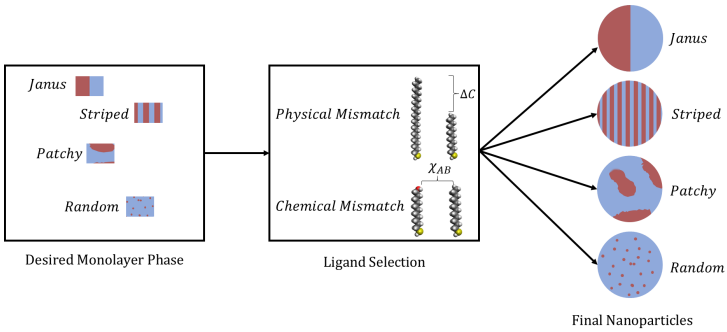

Figure 1.2: Illustration of how a set of design rules allows the desired monolayer phase separation to guide ligand selection. These design rules allow design of the desired phase separation in the synthesized nanoparticle and therefore the desired properties of that monolayer morphology.

Chapter 2

Merging Experiment and Theory

Developing an Experimental and Computational Characterization Technique for Noble Metal Nanoparticle Monolayers

This chapter was adapted from: Farrell, Z.; Merz, S.; Seager, J.; Dunn, C.; Egorov, S.; Green, D. L. Development of Experiment and Theory to Detect and Predict Ligand Phase Separation on Silver Nanoparticles. Angew. Chemie Int. Ed. 2015, 54 (22), 6479-6482.

2.1 Introduction

To develop our method, we analyze silver metal nanoparticles with an alkanethiolate monolayer. This system was chosen as an ideal candidate since noble metals are easily functionalized by alkanethiolates. Additionally, alkanethiolate monolayers on flat noble metal surfaces have been extensively studied in the past [19], which gives us a solid framework for predicting the expected behavior of the nanoparticle monolayer. The silver nanoparticles are synthesized using a one-phase one-step synthesis carried out in ethanol developed by Farrell et al. [20]. To evaluate our ability to detect phase separation we look at two multi-ligand monolayers. The first monolayer consists of dodecanethiol (DDT) and deuterated dodecanethiol ($[D_{25}]$DDT). As there is only an isotopic difference between these ligands we expect no phase separation to occur. The second monolayer consists of DDT and butanethiol (BT). We expect that this monolayer should undergo phase separation based on the physical mismatch between the two ligands. The phase separation induced by this physical mismatch is predicted by several previous computational studies [21–25] and is driven by the increase of entropy that results from maximizing free volume of the ligands [23].

2.2 Experimental

Silver nitrate (99.9999%purity), sodium borohydride (99.99%), 1- Butylphenyl)-2-methyl-2-propenylidene]malononitrile dodecanethiol ($\geq$ 98%), 1-butanethiol (99%), and trans-2-[3-(4-tert-Butylphenyl)-2-methyl-2-propenylidene]malononitrile (DCTB,$\geq$ 99.0%), were purchased from Sigma-Aldrich. Absolute ethanol and toluene (ACS reagent grade) were purchased from Fisher Scientific. Deuterated 1-dodecanethiol ([D25]dodecanethiol, 98.9 atom% deuterium) was purchased from C/D/N Isotopes. All reagents were used with no further purification. Ultrathin ($<$ 3nm) carbon film on 400 mesh copper holey carbon grids for TEM imaging were purchased from Ted Pella.

Mixed self-assembled monolayer Ag nanoparticles were synthesized by our direct method with the molar ratio of thiol ligand to silver nitrate held constant at 12 throughout all syntheses while varying the individual thiol concentrations in a given pair [20]. Silver nitrate was maintained at 0.5 mM in ethanol in all reactions and sodium borohydride was kept at a 12-fold excess at 6 mM. After initiation of the reaction by combining the reagents, the mixture was stirred for 30 min and then transferred to centrifuge tubes and centrifuged at 12000 rpm for 20 min. Following centrifugation, the supernatant was decanted and replaced with fresh ethanol. Subsequently the nanoparticles were redispersed by sonication and were again centrifuged. This was repeated three times and after the third and final centrifugation the nanoparticles were redispersed in toluene.

Nanoparticle samples were characterized using TEM and MALDI mass spectrometry. All TEM images were taken with an FEI Titan at an accelerating voltage of 300 kV. A drop-mounting method was used to prepare TEM samples. A TEM grid was held within self-closing tweezers and a pipette used to place a drop of nanoparticle solution onto the grid. A small piece of filter paper was used to wick away extra solvent and the grid was dried for at least one hour. Determination of nanoparticle size was performed using automated routines built into ImageJ software. MALDI measurements were performed on a Bruker MicroFlex. To prepare solutions for spotting onto a MALDI plate, trans-2-[3-(4-tert-butyl-phenyl)-2- methyl-2-propenylidene]malononitrile (DCTB; 0.025 g) were dissolved in 1 mL of nanoparticle solution. 100 mL of this solution was spotted per well of a standard ground-steel Bruker MALDI plate. Laser power was kept at 40% across all measurements with the detector operated in linear mode. Individual ion counts were calculated by integrating the area under the peak of interest using the trapezoid rule; in every case, these values were calculated for each ion of interest in the Ag_6L_5 series.

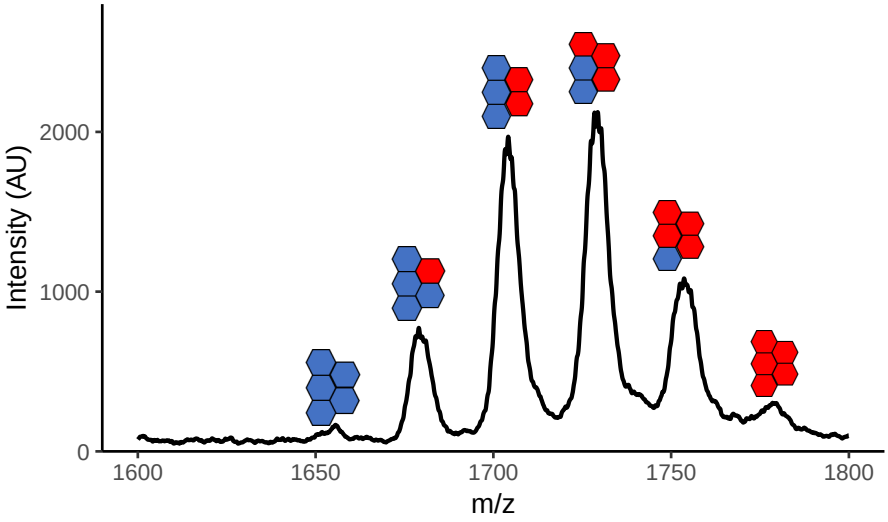

Figure 2.1: MALDI spectrum of the Ag_6L_5 fragment from Ag nanoparticles functionalized with DDT and its deuterated analogue [D25]DDT. Depicted above the spectrum are the number of DDT (blue) and [D25]DDT (red) ligands on a fragment corresponding to each MALDI peak.

2.3 Results and Discussion

The experimental technique employed is MALDI mass spectrometry, an ensemble-based method which produces mass spectra of solid analytes through ionization with a UV laser, thereby accelerating analyte fragments towards a detector that typically resolves species by time-of-flight.[8] This technique has general utility for metallic nanoparticles, but we currently employ only silver as well as a further study of gold (in the Supporting Information). In the case of silver, fragments are produced, with a generic formula of $Ag_{n+1}L_n$ where n is the number of ligands (L) on a fragment with $n+1$ Ag atoms [26]. We chose to analyze the Ag_6L_5 fragment family as it was prevalent in every spectrum and its peaks provide good resolution. The parameter L represents ligands, one being dodecanethiol (DDT) and the other being deuterated DDT ([D25]DDT) or butanethiol (BT). Analysis of the fragment provides a representative measure of the mol% of DDT, [D25]DDT, and BT on the surface as well as the monolayer phase separation. (For a detailed comparison of the Ag_6L_5 ion family with others, see the Supporting Information). Figure 2.1 shows the MALDI spectrum for the Ag_6L_5 fragment from silver nanoparticles functionalized with a 49 : 51 mol% mixture of adsorbed DDT and its deuterated analog [D25]DDT, respectively.

Anticipating that the Ag_6L_5 fragment provides a representative sampling of the surface, it is possible to create a frequency distribution. In the case of Ag_6L_5 with dodecanethiol as one of the two ligands, it is convenient to conceptualize each of the six possible ions in terms of how many DDT are present in each fragment (i.e., $0-5$ ligands). Knowledge of the frequency distribution also facilitates the computation of the relative amounts of each ligand, enabling a calculation of the binomial distribution, which would be expected for random ligand mixing. By comparing the experimental frequency distribution with the binomial distribution in Equation 3.1b (discussed below) it is possible to calculate a sum of squared residuals (SSR) between them, which is then representative of the degree of ligand phase separation. Random mixing is anticipated for the DDT/[D25]DDT monolayer; indeed, its frequency distribution coincides with the binomial distribution in Figure 2.2b.

Calculations on the volume-fraction profiles from the Scheutjen-Fleer self-consistent mean-field lattice model (SCF) [27] were used to simulate a theoretical spectrum, which could be compared to that obtained experimentally using MALDI mass spectrometry. It is appropriate to employ the SCF adsorption theory to model ligand interactions on silver as the SAM has a graft density approaching 5 $\frac{\text{ligands}}{\text{nm}^2}$ [28], equating to the concentrated brush regime where the mean-field approximation applies [29]. Further approximations were made to speed up computations: Although silver nanoparticles are faceted icosahedrons [30], the particle geometry was modeled as a pixelated sphere, permitting analyses to be carried out in Cartesian coordinates. Moreover, each ligand monomer fills a lattice site of constant size, thus ligand and solvent monomers are the same size in the simulations. To this end, three species are considered: the solvent and two chemically distinct ligands whose effective interaction are modeled by a Flory parameter, χ. The NP diameter was set to 20 lattice units, equivalent to the actual NP size of $3-4$nm, [20] and the number of monomers in a ligand were equated to the same number on the lattice; thus, dodecanethiol and butanethiol, respectively, are twelve and four lattice monomers long. An additional parameter is the dimensionless surface coverage, q, which we set to $q = 0.44$, equating to full monolayer coverage. The adsorbed ligand concentrations in the simulations were varied by changing the ratio of the two ligands on the surface. Subsequently, the resulting SCF calculations were compared to the MALDI results with a similar ligand ratio. The SCF calculations were carried out subject to the constraints of the minimization of the free energy and the conservation of mass. The resulting equilibrium volume-fraction profiles were determined by solving the polymer diffusion equation for each species with the appropriate boundary conditions, where each ligand was pinned and allowed to move around the interface. The current SCF formalism does not account for inter-chain crystallization known to occur in alkane thiols with carbon lengths $C \geq 10-12$ [31]. The agreement between theory and experiment below indicate that although the effects of inter-chain crystallization may be present, their influence is minimal on the random mixing between

DDT/[D25]DDT and phase separation between monolayers of DDT and much shorter butanethiol(BT) chains.

To simulate a MALDI spectrum, statistical analysis was performed on the monomer of each ligand pinned at the interface to mimic tracking of the Ag_6L_5 fragment. In particular, the two species of ligands on the fragment result in six peaks on a MALDI spectrum, representing the six possible binomial combinations. To simulate this distribution, a histogram was calculated from the probability, $P_{w,i}$, which was computed by summing the probability at each lattice space that was treated locally as a binomial of the six possible ligand combinations as weighted by the local volume fractions of the pinned monomers. The probability, $P_{w,i}$, is shown in Equation 2.1, where $i = 0 \dots n$, is the number of fragments out of a total of $n = 5$ fragments of the first ligand species; this species is DDT. The ligand volume fraction is ϕ and the subscript B denotes tracking of the other ligand species; the total interfacial concentration of DDT and species B is considered when ϕ includes the subscript T. The subscript, $k = 1 \dots M$, is an index for each ligand site for a total number of sites M. Equation 2.3 displays the SSR, which is determined by squaring and summing the residual, $P_{w,i} - P_{bi,i}$, where $P_{bi,i}$ is the binomial distribution in Equation 3.1b.

$$P_{w,i} = \frac{\sum_{k=1}^{M} (\phi_{DDT_k} + \phi_{B_k})^n \binom{n}{i} \phi_{DDT_k}^i \phi_{B_k}^{n-i}}{\sum_{k=1}^{M} (\phi_{DDT_k} + \phi_{B_k})} \tag{2.1}$$

$$P_{bi,i} = \binom{n}{i} \phi_{DDT_T}^i \phi_{B_T}^{n-i} \tag{2.2}$$

$$SSR = \sum_{i=1}^{n} (P_{w,i} - P_{bi,i})^2 \tag{2.3}$$

To connect experiment and theory, we analyzed the MALDI distributions of monolayers composed of DDT, an alkanethiol with 12 carbons, in combination with butanethiol (BT), a shorter alkanethiol with four carbons, or deuterated dodecanethiol [D25]DDT. One purpose is to use MALDI and SCF to establish the existence of phase separation for the DDT/[D25]DDT and DDT/BT mixed monolayers, which should result in well-mixed or striped monolayer, respectively. Well-mixed monolayers are anticipated for the DDT and [D25]DDT coated nanoparticles as a result of the chemical similarity of the ligands. Striped monolayers should result from the microphase segregation of DDT and BT, promoted by an increase in the conformational entropy of the longer ligand. A Flory parameter of $\chi_{CH_2} = 0$ was chosen to model the athermal interaction between the methyl and methylene groups of DDT, [D25]DDT, BT, and a simulated ethanol solvent. The Flory parameter between the hydroxy group of ethanol and the methyl and methylene groups of the ligands was set at $\chi_{CH_2/OH} = 2.0$.

Figure 2.2 shows the comparison between the MALDI spectra for the 50/50 mol% DDT/[D25]DDT and DDT/BT monolayers and the corresponding SCF predictions. The SCF images display the locations for DDT in blue and the opposing ligand in red. Thus, the color of the well-mixed monolayer is uniform, that is, one color, denoting random mixing in Figure 2.2a. This random mixing is supported by the correspondence between the MALDI and SCF spectra for DDT and [D25]DDT in Figure 2.2b where random mixing is indicated by the higher probability of having silver fragments with either two or three DDT ligands. In contrast, Figure 2.2c illustrates microphase separation and striped nanoparticle formation for semimiscible ligand mixtures, which is also supported by the agreement between the simulated and experimental spectra for DDT and BT in Figure 2.2d.

Although the error in the MALDI data is not shown in Figure 2.2 for clarity, variance in the data is due to random fluctuations in ligand ordering and error resulting from small variations in the triggering time or accelerating voltage in the MALDI system. Error in peak alignment is typically measured to be on the order of 0.1%, [32] which is anticipated to be smaller than random error. Hence, the standard deviation (σ) resulting from random fluctuations was estimated by comparing the spectra of the well-mixed monolayer DDT/[D25]DDT to the binomial distribution through $\sigma = \sqrt{\frac{\mathrm{SSR}}{j-1}}$ for $j = 84$ peaks yielding $\sigma = 0.04$, indicating that the peaks derived experimentally from MALDI mass spectrometry deviate from those calculated using SCF by 4%.

A plot of the SSR in Figure 2.3 provides another measure of ligand phase separation by quantifying the deviation from random mixing. To this end, we employed a one-step reaction scheme [20] to synthesize silver nanoparticles with monolayers of DDT and [D25]DDT as well as DDT with BT to detect the effect of differences in the carbon chain length in the ligands, ΔC, on phase separation over a range of interfacial concentrations. As a result of their chemical similarity, low SSR values from SCF and MALDI are anticipated for the DDT/[D25]DDT monolayer with ΔC= 0. For example, the SSR values from SCF are negligible (SSR $\approx 10^{-19}$,i.e., smaller than the relative error caused by rounding in floating-point arithmetic). Thus, the SCF calculation for favorably interacting, similar-sized ligands converges to the binomial distribution in Equation 3.1b, supporting our choice of this distribution to model a well-mixed monolayer. The experimental SSR values for the DDT/[D25]DDT monolayer are low, on the order of $10^{-3} - 10^{-2}$, similar to values obtained with MALDI for randomly-mixed monolayers by Cliffel and co-workers. [33] The SSR values should increase with monolayers of DDT and BT with ΔC= 8, as microphase separation is expected to occur for alkanethiol mixtures with a sufficient chain-length difference through gains in mixing entropy. [34] The SSR values obtained from MALDI experiments for DDT/BT monolayers increase 10-fold in comparison to the well-mixed case ($10^{-1} \gg 10^{-2}$). The theoretical

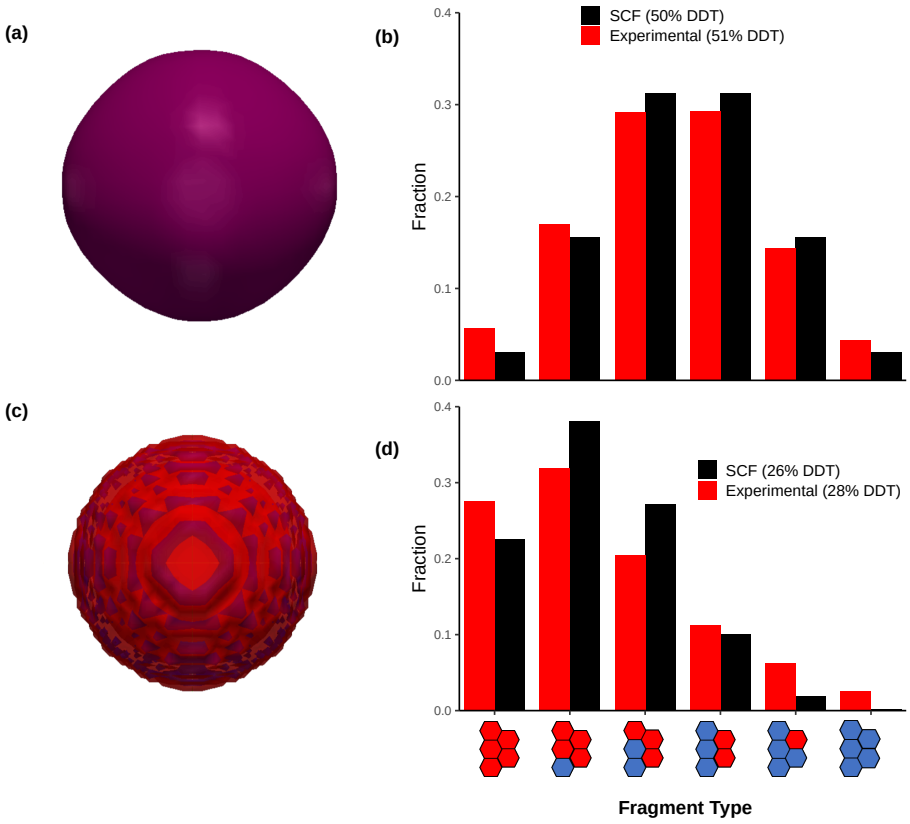

Figure 2.2: Comparison between the MALDI mass spectra and SCF predictions. (a) SCF image of well-mixed monolayer with simulated dodecanethiol (DDT) in blue and [D25]DDT in red, colors mix as purple. (b) MALDI spectra for the well-mixed DDT/[D25]DDT monolayer functionalized Ag nanoparticles and the corresponding SCF prediction. (c) SCF image of the striped nanoparticle with simulated DDT in blue (overlapping with red to give purple) and butanethiol (BT) in red. (d) MALDI spectra for microphase separated DDT/BT monolayer functionalized Ag nanoparticles and corresponding SCF prediction.

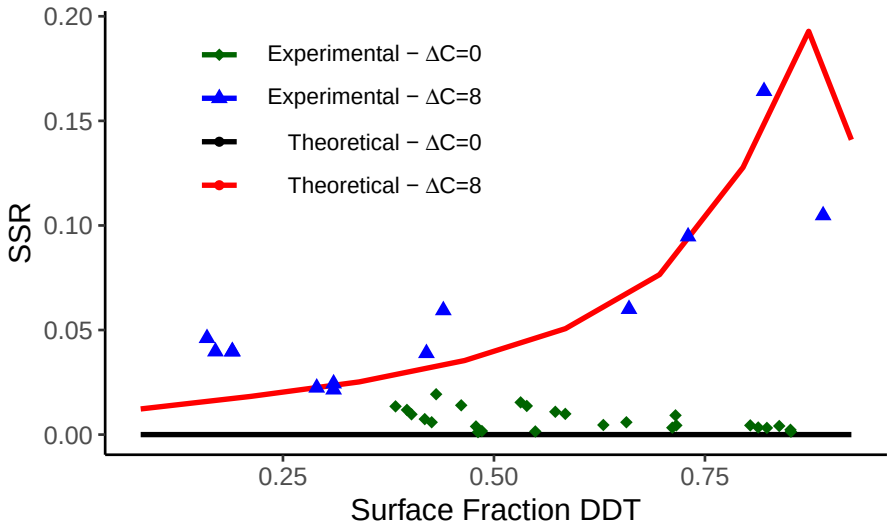

Figure 2.3: Comparison between experimental and theoretical SSR values from MALDI experiments and SCF calculations.

SSR value matches the trends and magnitude of the MALDI SSR, indicating good agreement between experiment and theory.

Through this work, we have demonstrated the ability to quantify and predict the phase separation of alkanethiols on Ag nanoparticles using MALDI and SCF as a function of both ligand concentration and carbon chain-length difference. These results indicate that, when pairing DDT with either its deuterated analogue [D25]DDT or BT, the SAM morphology progressed from a random ligand distribution to an intermediate degree of phase separation. We anticipate these methods will find utility in the design of nanomaterials with properties arising from phase-separated SAMs as they offer an inexpensive, high-throughput method for the measurement of ligand phase separation in nanoparticle systems.

Chapter 3

Exploring Stripey Monolayers

Investigation of Physical Mismatch on Phase Separation

This chapter was adapted from: Merz, S. N.; Farrell, Z. J.; Dunn, C. J.; Swanson, R. J.; Egorov, S. A.; Green, D. L. Theoretical and Experimental Investigation of Microphase Separation in Mixed Thiol Monolayers on Silver Nanoparticles. ACS Nano 2016, 10 (11), 9871-9878.

3.1 Introduction

Due to the high surface area-to-volume ratio of nanoparticles, controlling their interfacial chemistry is crucial to manipulating material properties. In particular, by functionalizing nanoparticle interfaces with specific monolayers, the electronic [35], optical [36], and chemical [14] properties can be modified for a variety of applications. Examples include uses in drug delivery [9], optics [36], and self- and directed-assembly [16,17,37]. In addition, researchers have shown that multi-ligand monolayers with phase separation can promote unique properties; for instance, ordered monolayers can penetrate cell membranes more easily [11] as well as dictate the assembly of anisotropic structures. [16] Hence, we seek to advance the field of interfacial engineering through the development of methods to detect and predict ligand phase separation on nanoparticle surfaces. A major thrust of the research is the facile synthesis of metallic nanoparticles such as silver (Ag) functionalized with ordered mixed ligand monolayers composed of dodecanethiol (an alkanethiol with 12 carbons) in combination with a second, shorter alkanethiol (having 4-11 carbons). Using Matrix Assisted Laser Desorption Ionization Mass Spectroscopy (MALDI), a technique typically used in the characterization of proteins and peptides but adapted by our lab for functional metallic nanoparticles, [38] we seek to systematically map the degree of phase separation for the nanoparticle monolayers produced by these alkanethiol combinations. MALDI combined with self-consistent mean-field theory (SCFT) calculations provide key details to the degree and type of

phase separation that occurs at the nanoparticle surface. Our results follow the transition from a well-mixed ligand monolayer to a microphase-separated monolayer, which occurs as the difference in chain length increases between the two adsorbed thiols.

Previous theoretical studies indicate a similar trend for alkanethiol mixtures with a sufficient chain length difference. [22, 24, 25, 34, 38, 39] There is also extensive experimental basis to complement the theoretical work, such as Stellacci's use of scanning-tunneling microscopy (STM) to detect monolayer morphology. However, aspects of this approach have recently been called into question. [40–43] Alternative methods of determining phase separation such as FTIR [44], NMR [45], and SANS [46] can provide some insight; however, these methods can be unreliable in dilute or polydisperse solutions. Hence, there is a great need for additional characterization techniques to complement the current theoretical and experimental framework, and the complementary use of MALDI and SCFT offers robust alternatives. Recent work within our group has shown that MALDI provides reproducible results, which correspond to predictions from SCFT [38]. In this paper we extend the use of MALDI and SCFT to systematically elucidate the effect of chain length difference on monolayer phase separation for homologous alkanethiol mixtures.

3.2 Experimental

Silver nitrate (99.9999% trace metals purity), sodium borohydride (99.99% trace metals purity), 1-dodecanethiol ($\geq$ 98% purity), 1-undecanethiol (98% purity), 1-decanethiol (96% purity), 1-nonanethiol (95% purity), 1-octanethiol ($\geq$ 98.5% purity), 1-hexanethiol (95% purity), 1-pentanethiol (98% purity), 1-butanethiol (99% purity), 2-mercaptoethanol ($\geq$ 99% purity), and trans-2-[3-(4-tert-Butylphenyl)-2-methyl-2-propenylidene]malononitrile (DCTB, $\geq$ 99.0% purity) were purchased from Sigma-Aldrich. 1-heptanethiol (98% purity) was purchased from Alfa-Aesar. Ethanol (absolute, molecular biology grade) and toluene (certified ACS reagent grade) were purchased from Fisher Scientific. Deuterated 1-dodecanethiol (dodecanethiol[D25], 98.9 atom% deuterium) was purchased from C/D/N Isotopes. All reagents were used with no further purification. Ultrathin ($>$ 3 nm) carbon film on 400 mesh copper holey carbon grids for TEM imaging were purchased from Ted Pella.

Mixed self-assembled monolayer Ag nanoparticles were synthesized via our direct method [20] as well as via a ligand exchange reaction reported by Hutchison. [47] For the direct method, the molar ratio of thiol ligand to silver nitrate, S, was held constant at 12 throughout all syntheses while varying the individual thiol concentrations in a given pair. Dodecanethiol was used in every synthesis while the second ligand was chosen from a homologous series of thiols: dodecanethiol[D25], undecanethiol, decanethiol, nonanethiol, octanethiol,

heptanethiol, hexanethiol, pentanethiol, butanethiol, or mercaptoethanol. Silver nitrate concentration was maintained at 0.5 mM in ethanol in all reactions and the concentration of sodium borohydride kept at a 12-fold excess, 6 mM. After reaction initiation via combination of the starting reagents, the reaction mixture was allowed to stir 30 minutes and then transferred to centrifuge tubes and centrifuged at 12000 RPM for 20 minutes. Following centrifugation, the supernatant was decanted and replaced with fresh ethanol, subsequently the nanoparticles were redispersed via sonication and again centrifuged. This was repeated three times, and after the third and final centrifugation the nanoparticles were redispersed in toluene instead of ethanol.

Nanoparticle samples were characterized using transmission electron microscopy (TEM) and matrix assisted laser desorption ionization mass spectroscopy (MALDI). All TEM images were taken with an FEI Titan at an accelerating voltage of 300 kV. Sample preparation of the TEM grids was done by a drop mounting method. A TEM grid was held within self-closing tweezers and a pipette used to place a drop of nanoparticle solution onto the grid. A small piece of filter paper is used to wick any extra solvent away and the grid dried for at least one hour. Determination of nanoparticle size was performed using automated routines built into the freely available ImageJ software developed by the National Institutes of Health. MALDI measurements were performed on a Bruker MicroFlex. To prepare solutions for spotting onto a MALDI plate, 0.025 grams of DCTB were dissolved in 1 mL of nanoparticle solution. 100 μL of this solution was spotted per well of a standard ground steel Bruker MALDI plate. Laser power was kept at 40% across all measurements with the detector operated in linear mode. Individual ion counts were calculated by integrating the area under the peak of interest using the trapezoid rule; in every case, these values were calculated for each ion of interest in the Ag_6L_5 series. These values were compared to a predicted binomial distribution produced from the surface concentrations of the two ligands as measured by MALDI, and the residual sum of squares error (computed as a measure of phase separation) [33].

SCFT simulations were run using SFBOX, a SCFT program created by Frans Leermakers et. al. The simulation was run with periodic boundary conditions in a cubic lattice with dimensions $61 \times 61 \times 61$ lattice units. The nanoparticle consists of surface monomers that have an athermal attraction to all other monomers and is centered in the simulation box with a diameter of 20 lattice units. Since the distance between lattice sites is equivalent to a carbon-carbon bond ($\sim$ 0.154 nm), this corresponds to a nanoparticle diameter of 3.08nm and a simulation box size of 9.39nm$\times$9.39nm$\times$9.39nm. The self-consistent equations underlying the Scheutjen and Fleer SCFT were solved using the SFBOX L-BFGS algorithm using a maximum acceptable error of 10^{-7}.

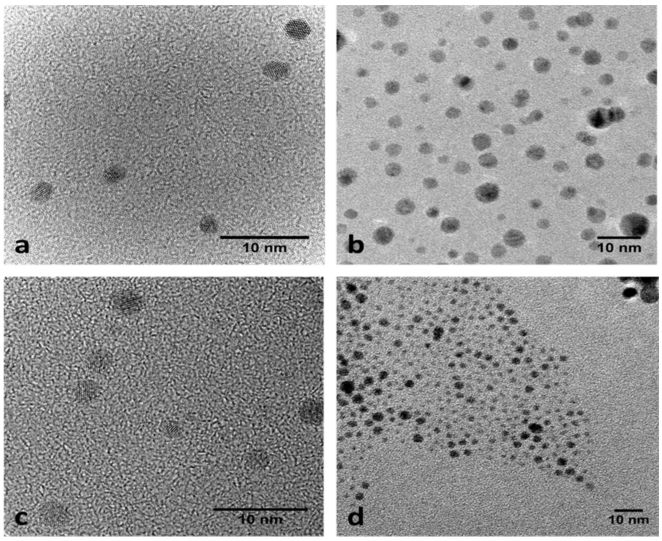

Figure 3.1: TEM images of (a) dodecanethiol/dodecanethiol[D25], (b) dodecanethiol/butanethiol, (c) dodecanethiol/octanethiol, and (d) dodecanethiol/mercaptoethanol mixed monolayer silver nanoparticles. All syntheses resulted in uniform nanoparticles with diameters ranging from $3-4$ nm, with a slight increase in diameter observed as the ligand paired with dodecanethiol was shortened (and thus decreased the average SAM thickness). Additional TEM images for ligand pairs not pictured above are found in Figure A.1 in the Appendix.

3.3 Results and Discussion

Silver (Ag) nanoparticles functionalized with a two-component monolayer of dodecanethiol and another alkanethiol, ranging between $4-12$ carbons, were prepared according to the synthesis laid out in a previous paper. [20] All nanoparticle samples were imaged with TEM to verify that they appear roughly spherical and relatively uniform in size to increase confidence that measurements of phase separation are due primarily to the differences in length and concentration of ligands and not variations in particle size or shape. TEM images for dodecanethiol/dodecanethiol[D25], dodecanethiol/octanethiol, and dodecanethiol/butanethiol are shown in Figure 3.1, which are representative of the mixed-monolayer functionalized nanoparticles examined in this work. TEM images for the remaining ligand pairs are reproduced in the Appendix as Figure A.1.

Subsequently, the functionalized materials were subjected to testing with MALDI, which fragments the nanoparticles while preserving local ligand structure, enabling quantification of the nearest-neighbor ligand distribution. [33] The resulting distribution can be compared to a theoretical prediction, such

as that from SCFT or a binomial distribution — the latter is expected to occur when ligands distribute randomly across the surface. [33] The sum-of-squares residual (SSR), or the summed amount of deviation between the binomial model prediction and the measured ion distribution, correlates to the degree of phase separation in the ligand monolayer. Using MALDI to characterize nanoparticle monolayers [33, 48–50], Cliffel and co-workers found that thiol-functionalized Au nanoparticles fragment in a particular pattern, M_nL_n which contains one ligand, L, per each metal atom, M, and a particular fragment, Au_4L_4, accounted for most of the mass spectrum [49]. In contrast, we have shown the tendency of thiol-functional Ag nanoparticles to fragment into ions of +1 charge whose formula can be generalized as $Ag_{n+1}L_n$ [38]; a similar pattern was also observed by Odriozola and co-workers in a MALDI-TOF study of silver hydrogels [26]. Throughout the experiments described in this paper, we chose to single out Ag_6L_5 fragments, as they were most abundant. A schematic of the MALDI process is shown in Figure 3.2.

The MALDI-TOF measurements were conducted on the functionalized nanoparticles as outlined in the Methods section. To quantify ligand distribution, the mass spectra were analyzed by determining the mass-to-charge ratios (m/z) at which each of the Ag_6L_5 ions appear, and then numerically integrating the area under those peaks. The index i is used to track each fragment peak over a total of $n = 5$ peaks. The peak values, c_i, were then normalized by the total area count, $\sum_{i=0}^{n} c_i$, yielding normalized peak values, θ_i, which can then be used to determine the surface fraction, x_i, of each ligand, e.g., dodecanethiol (DDT) - x_{DDT}, by finding the average number of that ligand in each fragment as shown in Equation 3.1a. Thus, the surface fraction, x_{DDT}, is the weighted average of the number of ligands of DDT in each fragment divided by the total number of ligands in the fragment family.

The normalized fragment peaks can then be analyzed to determine if the two ligands are uniformly distributed throughout the NP monolayers as each fragment can be thought of as a series of Bernoulli trials. A Bernoulli trial is a random experiment that has two possible mutually exclusive outcomes. Since each ligand in the Ag_6L_5 fragment has two mutually exclusive options, ligand A and ligand B, if the two ligands are randomly distributed then each ligand choice will behave as a Bernoulli trial. As the fragment contains several ligands the possible fragment choices are modeled as a series of Bernoulli trials which result in a binomial distribution, $\theta_{i,\mathrm{bin}}$, in Equation 3.1b. The Ag_6L_5 fragment contains five ligands and therefore can be modeled as a series of five Bernoulli trials as long as the surface is randomly mixed. However, if the surface is not randomly mixed then the ligand choices will not behave as a Bernoulli trial and the fragment distribution will deviate from the binomial distribution.

To find the expected binomial distribution we take that the probability of choosing a ligand is proportional to its concentration on the surface of the NP.

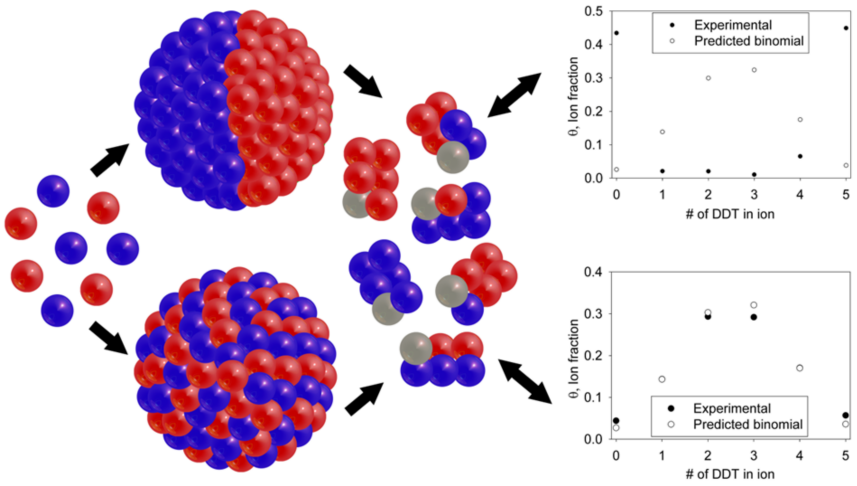

Figure 3.2: Schematic of potential nanoparticle self-assembled monolayer morphologies and subsequent fragmentation and measurement via MALDI. Starting from a mixture of two ligands (red and blue spheres), a self-assembled monolayer is formed on the surface of a nanoparticle. For ligands with extreme chemical and physical differences, phase separation is expected to result in a hemispherically separated or Janus morphology (top spectrum). For ligands that are chemically and physically similar, no phase separation is expected, which will result in a random distribution of ligands (bottom spectrum). Fragmentation of these nanoparticles results in ions, of which some have the form Ag_6L_5 composed of six silver atoms and a combination of five ligands from the ligand pair chosen in a given experiment. Janus particles are expected to produce MALDI spectra, which show extreme deviation from the randomly distributed (binomial) model as in the top graph. Particles with randomly distributed ligand monolayers are expected to produce MALDI spectra, which closely agree with the randomly distributed (binomial) model as in the bottom graph.

Once we have the probability for randomly selecting a ligand, the standard formula for a binomial distribution of five Bernoulli trials is used to produce the expected binomial spectrum. The deviation of the experimental spectrum from the binomial spectrum is measured as the sum of the squared residuals (SSR) between the two spectrums. The SSR indicates how far the experimental system deviates from a completely random monolayer and thus is a proxy for

phase separation.

$$\theta_i = \frac{c_i}{\sum_0^n c_i}; \mathrm{x}_{\mathrm{DDT}} = \frac{\sum_0^n i\theta_i}{n} \tag{3.1a}$$

$$\theta_{i,bin} = \binom{n}{i} \mathrm{x}_{\mathrm{DDT}}^i (1 - \mathrm{x}_{\mathrm{DDT}})^{n-i} \tag{3.1b}$$

$$SSR = \sum_0^n (\theta_i - \theta_{i,bin})^2 \tag{3.1c}$$

We demonstrate an analysis of the data based on the spectrum in Figure 3.3, which corresponds to a nanoparticle coated with dodecanethiol (DDT) and its deuterated analog (DDT[D25]). Due to the chemical and physical similarities between these two ligands a random monolayer is expected, which makes it an ideal test case for the method. If the monolayer is random as we expect then its MALDI spectrum calculated by Equation 3.1a should match the prediction of the binomial distribution in Equation 3.1b. A comparison between the binomial and experimental spectrum is illustrated in Figure 3.3b. Using the SSR from Equation 3.1c to quantify the mismatch between the spectrum we arrive at a low SSR value of 0.002 for the DDT/DDT[D25] monolayer, which can be reasonably be taken as the baseline for random mixing. Above this baseline, the experimental SSR values are indicative of ligand phase separation.

Based on previous work [22, 24, 25, 38, 39, 51], it is expected that increasing the carbon number difference between ligand pairs, ΔC, will promote phase separation. Therefore, we expect SSR values to increase with decreases in the carbon number of the second ligand relative to DDT. To test this hypothesis, Ag nanoparticles were synthesized with mixed SAMs consisting of dodecanethiol paired with a ligand selected from alkanethiol homologues ranging from $4 - 12$ carbons (i.e. deuterated dodecanethiol, undecanethiol, decanethiol, nonanethiol, octanethiol, heptanethiol, hexanethiol, pentanethiol, and butanethiol). These ligands are chemically similar, but with either the same or decreasing carbon number relative to dodecanethiol; thus, increasing $\Delta\mathrm{C} = 0 - 8$ through the selection of shorter ligands should increase microphase separation, corresponding to maximizing the conformational entropy of the system through maximization the free volume of the longer ligand, leading to striped monolayers.

To interpret the MALDI results, SCFT simulations were performed to elucidate the effect of ligand length difference on ligand phase separation. The simulations provide valuable information about monolayer morphology including the monolayer patterning, which can be only inferred, but cannot be directly determined using ensemble-averaged techniques such as MALDI. The simulations consisted of three monomeric components:

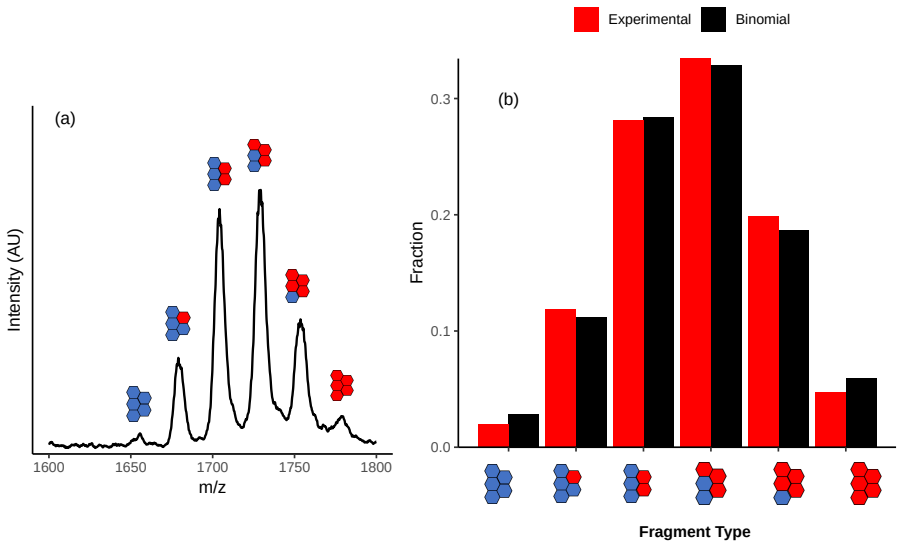

Figure 3.3: Example MALDI-MS spectrum and distribution (A) MALDI spectrum for the Ag_6L_5 fragment from Ag nanoparticles with dodecanethiol (DDT) /dodecanethiol[D25] monolayers; the five-octagon symbol above each peak represents the number of DDT ligands (in blue) or DDT[D25] ligands (in red) in an Ag_6L_5 fragment. (B) The experimental and predicted frequency distributions. The calculated sum of squares residual (SSR) is low at 0.002, which is anticipated for random ligand mixing.

1. Carbon monomers for the alkanethiols
2. Oxygen monomers for the solvent
3. Surface monomers for the nanoparticle surface.

The nanoparticle, surface was modeled as a pixelated sphere in Cartesian coordinates. The carbon and solvent monomers were used to simulate the following monolayer components:

1. Dodecanethiol - DDT
2. The corresponding alkanethiol - ALT
3. The solvent - SOL

The alkanethiols were created from the appropriate number of carbon monomers; thus, simulated dodecanethiol had 12 carbon monomers, and the numbers of carbons in the simulated alkanethiol homologues varied between $4-12$. To simulate the strong affinity between the metal and the thiol group of the ligand, the first monomers of the simulated ligands were pinned to the NP surface, but allowed to move along the NP surface. A Flory, or chi parameter, χ, of

$\chi_{OC} = 2.0$ between the solvent and the carbon monomers was chosen to reflect their chemical mismatch and is consistent with the values used in previous SCFT simulations. [52] The Flory parameter between alkanethiols was set to $\chi_{CC} = 0$, denoting athermal interaction which is expected between chemically identical monomers. The ratio of dodecanethiol to the shorter ligand was varied in the simulation to correspond to interfacial fractions from experiment. Similarly, the variance of the chain length difference of $\Delta C = 0 - 8$ in the two-component monolayer, matched the difference in carbon number between dodecanethiol and the other alkanethiol homologues used in the study. The ligand graft density in the simulations was set at 0.34 ligands/lattice site which corresponds to previous experimental values of grafting density of alkanethiols on gold nanoparticles [28] and is consistent with the grafting density values used in previous SCFT studies. [24, 38] Graft densities approaching $5 \frac{\text{ligands}}{\text{nm}^2}$ equate to the concentrated brush regime where the SCFT mean-field approximation applies. [29]

As described in our previous work, [38] we predicted the MALDI spectra from the ligand volume fraction profiles produced from SCFT calculations. To this end, the local lattice site surface fractions, θ_i, are found, which solve the polymer diffusion equation for each simulated species subject to the constraints of the minimization of the system free energy and the conservation of mass. To produce the predicted spectrum, each lattice site on the NP surface was treated as well mixed. Thus, the local mixing of dodecanethiol (DDT) with another alkanethiol homologue (ALT) results in a binomial distribution in line with the local surface fractions of both species. The local distributions are then weighted by the local site densities of both ligands raised to the fifth power to capture the probability of finding five ligands near each other in the lattice site. This yields the predicted spectrum, θ_i, SCFT as shown in Equation 3.2a where $i = 0 \ldots n$ is the ligand index with $n = 5$ ligands per fragment, and ligand lattice surface sites are denoted by the index $k = 1 \ldots M$ for a total of M sites.

$$\theta_{i,SCFT} = \sum_{k=1}^{M} \frac{(\phi_{DDT_k} + \phi_{ALT_k})^n \binom{n}{i} x_{DDT_k}^i x_{ALT_k}^{n-i}}{(\phi_{DDT_k} + \phi_{ALT_k})^n} \tag{3.2a}$$

$$x_{DDT_k} = \frac{\phi_{DDT_k}}{\phi_{DDT_k} + \phi_{ALT_k}} \tag{3.2b}$$

$$x_{ALT_k} = \frac{\phi_{ALT_k}}{\phi_{DDT_k} + \phi_{ALT_k}} \tag{3.2c}$$

$$SSR = \sum_{0}^{n} (\theta_{i,SCFT} - \theta_{i,bin})^2 \tag{3.2d}$$

The theoretical SSR in Equation 3.2d is produced by comparing θ_i, SCFT from Equation 3.2a, to $\theta_{i,\text{bin}}$ from Equation 3.1b. Comparisons between the experimental and theoretical frequency distributions (Equation 3.1a and Equa-

tion 3.2a) and sum-of-squares residuals (the SSR in Equation 3.1c and Equation 3.2d) allow us to better gauge how well the computational results reflect the experimental system. In the case of random ligand mixing, the θ_i, SCFT, will converge to θ_i, bin resulting in a SSR near zero. This is consistent with the experimental SSR= 0.002 of the well-mixed system in Figure 3.3. In our previous work [38] we synthesized Ag nanoparticles functionalized with monolayers of dodecanethiol (DDT) with either deuterated dodecanethiol (DDT[D25]) or butanethiol (BT), and we used MALDI and SCFT to detect and predict the effect of carbon number difference at ΔC = 0 and ΔC = 8 on ligand phase separation while spanning a wide range interfacial ligand fractions from $x_{DDT} = 0.05 - 0.90$. The SCFT predictions corresponded well with the spectra and SSR from MALDI, indicating random mixing for the DDT/DDT[D25] monolayer and ligand phase separation and stripe formation for the DDT/BT monolayer. In particular in Figure 3.3 of the previous work [38] we plotted the experimental and theoretical SSR as a function of x_{DDT} to demonstrate a low $SSR = 0.002$ at ΔC = 0, and up to a two-order magnitude increase in SSR= $0.02 - 0.20$ at ΔC = 8 with a peak in the SSR observed at $x_{DDT} = 0.80$. In this paper we extend the previous work to more clearly determine the effect of ΔC on ligand phase separation with monolayers of DDT/DDT[D25] through DDT/BT to produce mixtures spanning $\Delta C = 0 - 8$. Further analysis will also bring about a better understanding of the possible range of patterning exhibited through the use of SCFT visualizations.

In Figure 3.5 of this manuscript, we continue to see the pattern of SSR peaking around $x_{DDT} = 0.80$ for the $\Delta C = 0 - 8$ monolayers. In addition, we also detect increasing phase separation, as quantified by the SSR, as the chain length difference increases from $\Delta C = 0 - 8$ as expected. To better show the effects of ΔC on phase separation, the SSR was plotted against ΔC for $x_{DDT} \approx 0.80$, the peak in the SSR at each ΔC, as shown in Figure 3.4. In addition, the SCFT SSR values for each ΔC at $x_{DDT} \approx 0.80$ are also plotted in Figure 3.4 to see how well SCFT captures the effect of ΔC on phase separation. The predicted SSR increase with ΔC, indicating greater phase separation in the monolayer, and a good correspondence is observed between experiment and theory.

The final comparison between all the experimental and SCFT SSR values is shown in Figure 3.5. While there are some minor disagreements the computational data captures the same trend of increasing SSR value with increasing chain length mismatch. In addition, the computational data shows a peak in SSR values near a concentration of 80% dodecanethiol on the surface which is also reflected in the experimental data. The minor disagreement between experimental and computational data may be due to minor differences in the nanoparticle shape between the simulation and the experiment as well as excluded volume effects which are not fully accounted for in the SCFT. Additionally, the SCFT simulation does not include the effects of chain crystallization

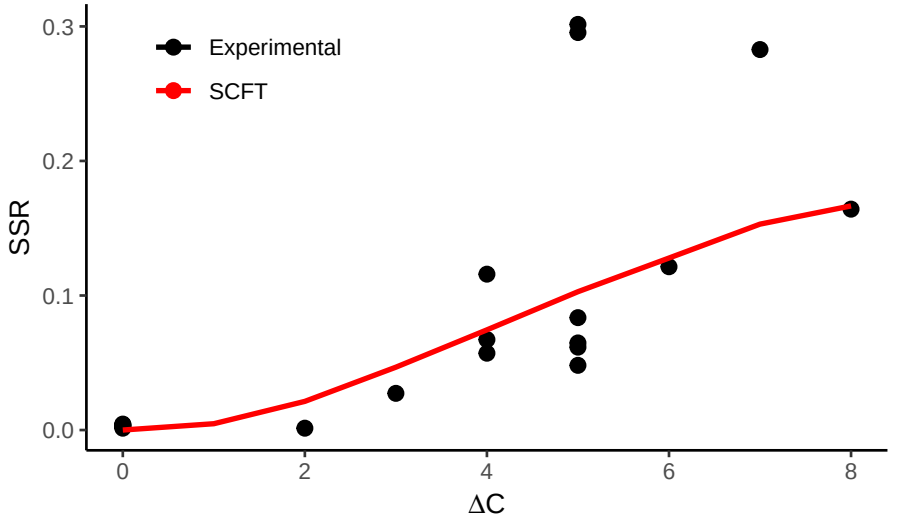

Figure 3.4: The trend in ligand phase separation around the maximum value of the sum-of-squares residual (SSR) as a function of the increasing chain length mismatch (ΔC) for interfacial dodecanethiol (DDT) fractions around $x_{DDT} \approx 0.80$.

which can become significant for alkanethiols of chain length 9 or more [53]. Despite these deficiencies the good agreement between computational and experimental results suggest that the SCFT simulation captures the major effects relevant to the nanoparticle monolayer (see Figure 3.4 and Figure 3.5).

In addition to the prediction of the SSR from MALDI, the SCFT simulations also provide predictions of the spatial volume fraction profiles of the monolayer shell, indicating the most thermodynamically favorable ligand arrangements, and thus, monolayer patterning. Figure 3.6 shows the pinned monomer of the ligands to indicate how the ligand distribution changes as a function of interfacial mole fraction of DDT (x_{DDT}) and the carbon length difference between DDT and the shorter alkanethiols, ΔC. Figure 3.6 illustrates the pinned monomer of the ligands to show how the ligand distribution changes as a function of interfacial mole fraction of DDT (x_{DDT}) and the carbon length difference between DDT and the shorter alkanethiols, ΔC. In Figure 3.6 the DDT volume fraction profile is shown in blue and the shorter ligand volume fraction profile is shown in red, mixing between the two profiles results in a purple color, which is observed in the bottom row. Consistent with the SSR value results the volume fraction profiles show a decrease in mixing (i.e., an increase in phase separation) as the chain length mismatch, ΔC, increases. One observes the increase in ligand phase separation in Figure 3.6 through the elevating intensity of DDT in blue while moving diagonally from the bottom left to the upper right. The nanoparticle monolayers that show the most phase separation at each chain

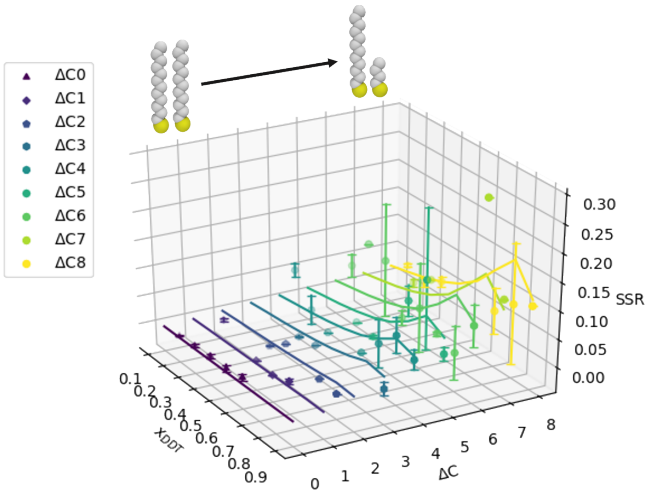

Figure 3.5: Comparison of sum-of-squares residual (SSR) from MALDI experiment (the symbols) and SCF theory (the lines). The parameter x_{DDT} is the surface fraction of dodecanethiol (DDT) and ΔC is the carbon number difference between DDT and shorter alkanethiol homologues from the study.

length mismatch occur at $x_{DDT} = 0.80$, which is in agreement with both the experimental and SCFT derived SSR values. It can also be seen that dodecanethiol segregates to the corner and edge sites of the nanoparticle surface as chain length mismatch increases. This is due to the larger free volume available at these sites, which provides a greater gain in conformational entropy to dodecanethiol ligands than the shorter ligands. This result is consistent with previous simulation work by Glotzer et. al. [23]

The volume fraction profiles can also be analyzed to determine the characteristic length scales of the stripes formed. The analysis was carried out by examining the variation of the corresponding alkanethiol, ALT, across the nanoparticle surface. Hence, the 3-D volume fraction values of x_{ALT} were projected onto the x-axis by summing the values across the y- and z-axis at each point on the x-axis and normalizing by the total number of surface sites, N_x, at that point in the x-axis, or $x_{ALT} = \frac{1}{N_x}\sum_y \sum_z x_{ALT_k}$. This process is illustrated in Figure 3.7 at $x_{DDT} = 0.80$. The flat profile for $\Delta C = 0$ is anticipated for random ligand mixing and the normalization results in $x_{ALT} = 0.20$ for a correct baseline. In contrast, the variation for $\Delta C = 8$ represents a length-scale dependent clustering of ligands on the nanoparticle surface.

To better quantify the characteristic lengths involved in the monolayer phase separation, Matlab was used to take the fast Fourier transform (fft) of $x_{ALT}(x)$

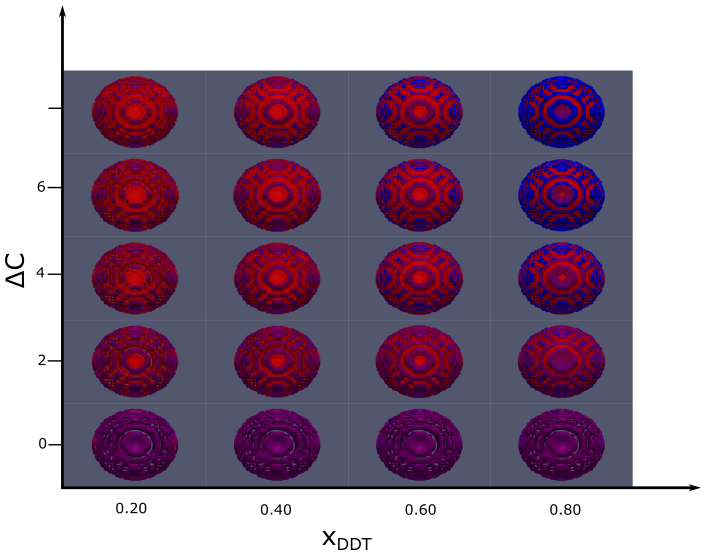

Figure 3.6: Predicted monolayer patterns from SCF theory as a function of carbon number difference, ΔC, and mol fraction of dodecanethiol (DDT), X_{DDT}. DDT is shown in blue and the corresponding shorter alkanethiol in red, only the pinned monomer of each ligand is shown to better show patterning at the nanoparticle surface. Areas of uniform random ligand mixing are denoted by the color purple upon mixing of colors red and blue.

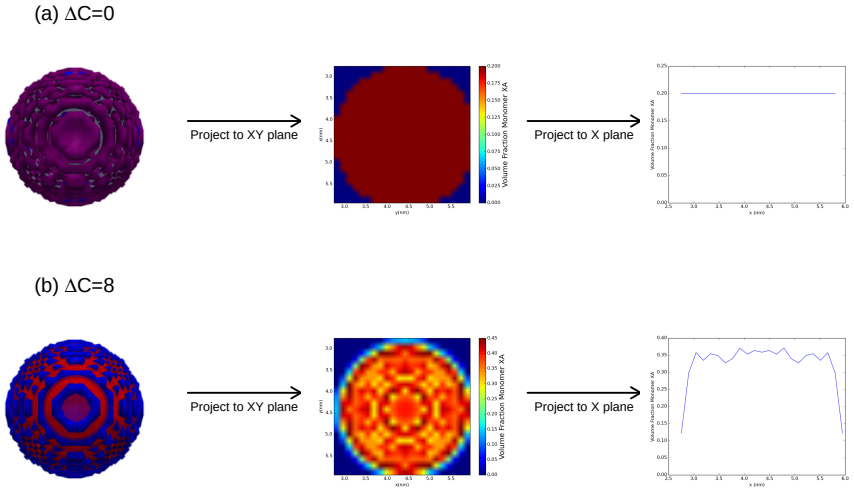

Figure 3.7: Demonstration of projection procedure for conversion of a 3-D SCF volume fraction profile to a 1-D distribution. The procedure, which is discussed in the text, is shown for (a) $\Delta C = 0$ and (b) $\Delta C = 8$ for $x_{DDT} = 0.80$.

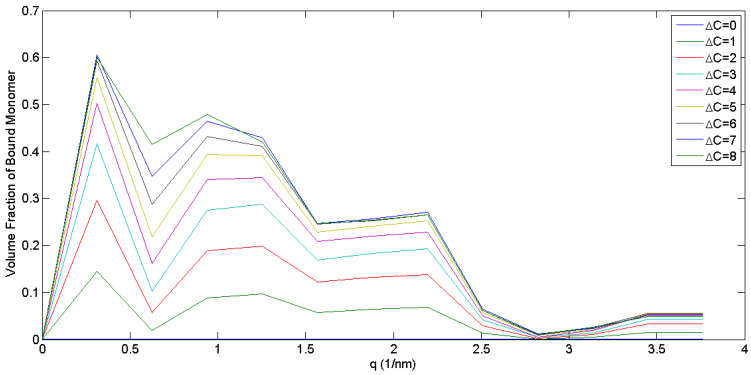

Figure 3.8: Fourier transform of the 1-D projections for each chain length difference, ΔC. Peaks are seen at inverse space points of 0.313, 0.9404 − 1.254, 2.194, and 3.5 nm^{-1}, which respectively corresponds to length scales of 3.19, 1.06 − 0.80, 0.46, and 0.29 nm.

for each ΔC in Figure 3.8 at $x_{_{DDT}} = 0.80$, corresponding to maximum phase separation. To focus solely on the deviations in the monolayer, we first subtracted the mean value of the volume fraction, $x_{_{avg,\Delta C}} = \frac{1}{N}\sum_{i=1}^{N}[x_{_{avg,\Delta C}}(x_i)]$ from the projection so that the Fourier transform stems from deviations from the mean value. Increasing intensity represents higher accumulation, and the length scale of each peak is given as $L = q-1$. The resolution of the fft is $0.313nm^{-1}$. Based on the Fourier transform the smallest length scale of monolayer variation is 0.29 nm, corresponding to the resolution limit of the lattice. Larger more prominent variations occur at 3.19, 1.06 − 0.80, and 0.46 nm. The 3.19nm, peak corresponds roughly to the diameter of the particle. This increase is related to the increasing concentration of corner and edge sites near the edge of the particle in the x-axis projection. This increasing concentration of higher free volume sites drives segregation of the longer chain to these sites which causes a sharp depletion of the shorter chain. This effect is shown in the 1D projection pictured in Figure 3.7b. The 1.06 − 0.80nm peak is consistent with the distance between stripes observed by Stellacci et. al. [54] Finally, the 0.46nm peak corresponds to the characteristic nearest neighbor distance of alkanethiols on silver. [55] The prominence of these peaks increases with ΔC as the chain length difference promotes stronger segregation.

3.4 Conclusion

Through this work we have demonstrated our ability to characterize several different mixed thiol monolayers using MALDI-TOF, SCFT, and TEM. The homologous nature of the ligands and the stepwise experimental changes have permitted us to utilize the MALDI method for detecting ligand phase separation in mixed SAMs to produce a detailed map of variation in phase separation as a function of both ligand concentration and chain length mismatch in our nanoparticle systems. These results indicated that when pairing dodecanethiol with one of a homologous series of alkanethiol ligands from deuterated dodecanethiol [D25] through butanethiol, the SAM morphology progressed from a random ligand distribution to microphase separation. Further information about the monolayer was gathered using SCFT simulations. The simulation results agree well with experimental results and provide additional information on the patterning of ligands in the monolayer.

Chapter 4

Exploring Patchy Monolayers

Characterization of Noble Metal Nanoparticles with Chemical Mismatch

This chapter was adapted from: Merz, S. N.; Farrell, Z. J.; Pearring, J.; Hoover, E.; Kester, M.; Egorov, S. A.; Green, D. L.; DuBay, K. H. Computational and Experimental Investigation of Janus-Like Monolayers on Ultrasmall Noble Metal Nanoparticles. ACS Nano 2018, acsnano.8b05188.

4.1 Introduction

Monolayer protected nanoparticles (NPs) have a wide variety of applications in photonics, [16, 36, 56–58] drug delivery, [59–62] radiotherapy, [63–67] and protein sensing. [68,69] Previous work has shown that multi-ligand monolayers can undergo phase separation, [33, 70–72] which can have a significant impact on the properties of both flat [71] and nanoparticle monolayers. [9, 59, 73, 74] Structured monolayers containing multiple types of ligands promise to increase the functionality of the NP monolayer. [7, 8, 13, 75, 76] For example, in drug delivery applications, NPs with patchy and Janus-like monolayer phases are better able to penetrate cell membranes, [9, 59, 75, 77] while also enabling the delivery of multiple agents into a cell. [8] The primary drivers for phase separation within these monolayers lie in the physical size and chemical composition mismatches between ligands.

In addition to ligand patterning, size can also play a key role in determining NP properties. Ultrasmall NPs, i.e. those less than 10nm, are particularly effective in radiotherapy, [64] and NPs with hydrodynamic diameters less than 5.5nm can be cleared from the body through the renal system, mitigating unwanted side-effects. [78] Noble metal nanoparticles are particularly attractive due to their relatively good biocompatibility. [79, 80] Ultrasmall NPs are also attractive options for gene therapy as their small diameter allows them to pass

into the cell nucleus. [81] However, in order to reliably design and synthesize ultrasmall NPs with the desired functional properties, we must first be able to accurately characterize their surface ligand morphologies.

Although the characterization of Janus particles larger than 20nm can be readily accomplished with traditional visualization techniques such as AFM, [82] STM, [54] and TEM, [83] characterizing Janus-like monolayers on ultrasmall NPs has proven difficult. Early attempts using STM were made by Stellacci et. al in 2004, [84] but this study has drawn controversy due to the complications inherent in imaging particles with a curvature comparable to that of the STM tip. [40–43] Cryo-TEM techniques have analyzed NPs with ligands containing large atomic weight atoms, such as polyoxometalate (POM) clusters, [85] however this technique is restricted to a particular set of ligands. As a result of these imaging limitations, several indirect experimental methods have been used to characterize nanoparticle monolayers, including FTIR, [44] SANS, [46,86] NMR, [45] and MALDI-MS. [33,38,87] These methods indicate the degree of mixing within the monolayer; however, they fail to give detailed information on its exact morphology. [41,42] FTIR and NMR detect the proximity of different functional groups within the multi-ligand monolayer through shifts in the spectrum, and SANS can provide information on the radial distribution of surface ligands by taking advantage of the contrast between deuterated and un-deuterated molecules. [41,42] Similarly, MALDI-MS examines the clustering of ligands on a small scale by finding the ratio of each ligand type within sampled clusters containing $4-5$ ligands. Although these techniques provide information on ligand spacing and clustering, a complete picture of the NP monolayer cannot be obtained from their data alone.

Numerical simulations can help fill in the missing information by providing insight on the various driving forces behind ligand phase separation as well as atomistically detailed information on expected monolayer configurations. Work by Glotzer et. al [34] and Stellacci et. al [86] used dissipative particle dynamics with a soft repulsive potential to model ligand monolayers. While these studies provide insight on the effects of physical and chemical mismatch on phase separation in the ligand monolayers, the simulations do not explicitly include attractive interactions between ligands or nanoparticle faceting, both of which have been shown to be important in subsequent work on NP [22,88] and flat [89] monolayer phase separations. Other groups have modelled NP monolayers using molecular dynamics. [88,90] However, the equilibration of thiol monolayers in the laboratory can take up to 4 days, [91] making it impossible for traditional molecular dynamics simulations to reach equilibrium. Our own previous work used self-consistent field theory (SCFT) to model the nanoparticle monolayer. [38,87] SCFT determines the equilibrium monolayer configuration by solving a set of self-consistent equations. Such calculations are free of the time scale constraints suffered by MD simulations. However, SCFT breaks down for systems with chemical mismatch, since typical implementa-

tions rely on simple, isotropic Flory-Huggins contact potentials. This isotropic potential cannot accurately describe important anisotropic intermolecular interactions, such as hydrogen bonding, that occur in chemically mismatched monolayers.

One of the main drawbacks of previous computational work is the lack of direct comparison to experimental measurements. Most computational studies involve a qualitative comparison between electron microscopy images from techniques such as STM and TEM and snapshots of the simulations. Recent work by Stellacci and coworkers works to bridge this gap through the use of simulated annealing to fit the location of various ligand head groups to experimental SANS data. [46, 86] Using this technique, Luo et al. analyzed several different monolayers with both chemical and physical mismatch on gold and copper metal NPs and were able to achieve a quantitative fit to SANS-derived pair distribution functions. A qualitative match between the fitted head group locations and DPD simulations was also found. The method outlined by Luo et al. shows promise as a versatile technique for characterizing nanoparticle monolayers. However, there are some drawbacks to this technique as SANS requires one of the head groups be deuterated, and a large polydispersity ($> 10\%$) can alter the form factor data, complicating interpretation. Finally, since the structural information primarily comes from fitting ligand locations to experimental data rather than from independent models designed to realistically represent the physical forces acting upon the ligands, extensions of this computational technique to prediction and design are limited.

In this work, we make use of advanced MC sampling algorithms on atomistic models to enhance our ability to interpret MALDI-MS results that report on multi-ligand monolayer organization for physically and chemically mismatched ligands. MALDI-MS can characterize the NP monolayers without modifying the NPs and can distinguish between a wide variety of head groups with only mass differences. Both computational and experimental results indicate that the synthesized NPs have a Janus-like monolayer, and the correspondence between the two lends credence to the atomistic insight provided by the simulations.

4.2 Methods

Experimental

Reagents and Materials

Silver nitrate (99.9999% trace metals purity), sodium borohydride (99.99% trace metals purity), 1-dodecanethiol ($\geq$ 98% purity), 1-butanethiol (99% purity), 2-mercaptoethanol ($\geq$ 99% purity), and trans-2-[3-(4-tert-Butylphenyl)-2-methyl-2-propenylidene]malononitrile (DCTB, $\geq$ 99.0% purity) were purchased from Sigma-Aldrich. 1-heptanethiol (98% purity) was purchased from

Alfa-Aesar. Ethanol (absolute, molecular biology grade) and toluene (certified ACS reagent grade) were purchased from Fisher Scientific. All reagents were used with no further purification. Ultrathin (< 3 nm) carbon film on 400 mesh copper holey carbon grids for TEM imaging were purchased from Ted Pella.

Nanoparticle Synthesis

Mixed self-assembled monolayer silver metal NPs were synthesized via our one-step synthesis method. [20] In brief, the molar ratio of thiol ligand to silver nitrate, S, was held constant at 12 throughout all syntheses while varying the concentration ratio between the two thiol types. Silver nitrate concentration was maintained at 0.5 mM in ethanol in all reactions and the concentration of sodium borohydride was kept at a 12-fold excess, 6 mM. After reaction initiation via combination of the starting reagents, the reaction mixture was allowed to stir 30 minutes and then transferred to centrifuge tubes and centrifuged at 12000 RPM for 20 minutes. Following centrifugation, the supernatant was decanted and replaced with fresh ethanol. Subsequently the NPs were redispersed via sonication and again centrifuged. This wash process was repeated three times, and after the third and final centrifugation, the NPs were redispersed in toluene instead of ethanol. To verify that the wash process successfully eliminated free ligands from solution an H NMR spectrum was taken after the three washes and compared with the H NMR spectrum of free ligands in solution. The H NMR showed no fine peaks with the peak broadening and shifting associated with thiols bound to metal nanoparticle cores. [92] The H NMR of the free ligands along with the washed nanoparticles is shown in Figure B.8.

Nanoparticle Characterization

Nanoparticle samples were characterized using transmission electron microscopy (TEM) and MALDI-MS. All TEM images were taken with a FEI Titan at an accelerating voltage of 300 kV. Sample preparation of the TEM grids was done by a drop mounting method. A TEM grid was held within self-closing tweezers and a pipette used to place a drop of nanoparticle solution onto the grid. A small piece of filter paper is used to wick any extra solvent away, and the grid dried for at least one hour. Determination of nanoparticle size was performed using automated routines built into the freely available ImageJ software developed by the National Institutes of Health. [93] MALDI-MS measurements were performed on a Bruker MicroFlex. To prepare solutions for spotting onto a MALDI-MS plate, 0.025 grams of matrix assist agent DCTB (trans-2-[3-(4-tert-Butylphenyl)-2-methyl-2-propenylidene]malononitrile) were dissolved in 1 mL of nanoparticle solution. 100μL of this solution was spotted per well on a standard ground steel Bruker MALDI-MS plate. Laser power was kept at 40% across all measurements with the detector operated in linear mode. Individual ion counts were calculated by integrating the area under the peak of interest using the trapezoid rule; in every case, these values were calculated for each ion of interest in the Ag_6L_5 series. The surface concentration of each

ligand on the surface can be calculated by weighting the concentration of the ligand with each fragment by the normalized area under each fragment peak. This is shown Equation 4.1 with χ_{DDT} being the surface fraction of DDT on the surface and A_i as the area of the Ag_6L_5 peak with i DDT ligands. These values were compared to a predicted binomial distribution produced from the surface concentrations of the two ligands as measured by MALDI, and the residual sum of squares error (computed as a measure of phase separation).

$$\chi_{DDT} = \frac{\sum_{i=0}^{5} A_i(\frac{i}{5})}{\sum_{i=0}^{5} A_i} \tag{4.1}$$

Computational

Atomistic Simulation

The atomistic simulation consists of a 4nm icosahedral nanoparticle made of silver atoms arranged in an FCC lattice with a lattice constant of 4.08$\AA$, which corresponds to the experimentally measured silver lattice constant. [94] The two ligands are represented by a united atom model. The united atom dodecanethiol is represented as 12 point particles, one for each carbon monomer, with one point particle for the sulfur atom. The mercaptoethanol is modelled as a point particle for the sulfur, carbon monomers, and the oxygen atom with the addition of a point particle for the hydrogen atom directly bonded to the oxygen atom, allowing for a more accurate representation of the hydrogen bonding interaction that occurs between mercaptoethanol molecules.

The force field for the atomistic simulation is the commonly used OPLS united atom force field. [95] Intermolecular interactions are modelled using a Lennard-Jones term, E_{LJ}, shown in Equation 4.2 with ϵ corresponding to the well depth of the potential, r representing the interatomic distance, and σ representing the point of zero potential between two atoms.

$$E_{LJ} = 4\epsilon[\left(\frac{\sigma}{r}\right)^{12} - \left(\frac{\sigma}{r}\right)^{6}] \tag{4.2}$$

Solvent molecules were not explicitly included, however a Debye screened Coulombic potential was used to model coulombic interactions and to capture the screening effect of the solvent. The form of the coulombic screened potential is shown in Equation 4.3 with q_i and q_j standing for the charges of two charged atoms i and j, r_{ij} representing the interatomic distance between the two atoms, ϵ the dielectric constant, κ the inverse Debye length, and C the Coulomb's constant. Based on the experimental salt concentration a Debye length, κ^{-1}, of 5Å was used.

$$E_{col} = \frac{Cq_iq_j}{\epsilon r_{ij}} e^{-\kappa r_{ij}} \tag{4.3}$$

The binding potential between sulfur and silver metal atoms was modelled as a Morse potential (see Equation 4.4) in keeping with previous modelling of alkanethiolates on noble metal surfaces. [53, 96–98] A well depth (D_ϵ) of 5.78 kcal/mol, equilibrium bond distance (r_o) of 2.87Å, and potential well width parameter $\alpha = 0.746$Å is used for the Morse potential and taken from previous DFT work examining silver thiolate binding. [99, 100]

$$\mathrm{E}_{morse} = D_\epsilon[e^{-2\alpha(r-r_o)} - 2e^{-\alpha(r-r_o)}] \tag{4.4}$$

Configurationally-biased Monte Carlo simulations were carried out via a Python program using LAMMPS [101] for energy evaluations. The move set consists of four different moves: translation, rotation, configurationally biased regrowth, and configurationally biased identity swap. This suite of moves was based on previous MC moves used to model alkanethiol monolayers. [102–104] Translation moves consist of a $0 - 5$Å translation of a randomly chosen ligand in the direction of a randomly chosen unit vector. The rotation move rotates a ligand about a randomly chosen axis centered at the sulfur atom to which the ligand is bound. The configurationally biased regrowth move regrows a ligand in place using the Rosenbluth weight which gives higher preference to more energetically favorable chain configurations. Finally, the configurationally biased identity swap move swaps the identity of two randomly selected ligands of opposite type and regrows them using configurationally biased regrowth. The use of configurationally biased regrowth biases selection to diminish the sampling of physically unrealistic chain collisions, greatly increasing acceptance rates of moves involving chain regrowth. This increased sampling efficiency becomes more important with the dense monolayers found in the experimental system as close packing causes most of the configurational space to be highly energetically unfavorable. Simulations were run at 298K as the experimental NPs are synthesized at room temperature. Simulations were run for 800,000 (800k) steps.

Equilibration

Results from six simulations run at $0.50\chi_{DDT}$ show that after 800k steps the acceptance rate of swap moves had remained near zero for over 100k steps. The near zero acceptance rate of swap moves over the period of 100k steps suggests that we have reached a stationary state by 800k steps, however this state may not be the equilibrium state. We achieve a high degree of confidence that our simulation has reached equilibrium using several different checks.

The first check to make sure each simulation reaches equilibrium was to run six simulations for every DDT surface fraction point. The six simulations were started from different randomly mixed initial configurations generated using the Packmol software. [105] Thus, if a similar final configuration is obtained across simulations it can be said with some degree of confidence that an equilibrium state has been reached. The final configurations were then characterized by

calculating an expected MALDI-MS distribution and its corresponding SSR_{sim} with respect to the binomial distribution expected from a totally randomly mixed monolayer. A small spread in the SSR values of the final configurations was taken as a quantitative measure of the convergence of the six random starting points.

While these results strongly suggest we have reached a stable configuration, it does not guarantee that we have sufficiently sampled the monolayer configuration phase space to find the true equilibrium. We also ran four additional simulations that began at different possible monolayer configurations, random, 5Å stripes, 10Å stripes, and Janus monolayers. For each morphology six trials were run. The configurations were compared using their SSR values after 800k steps. The SSR_{sim} comparison between simulations starting from different initial morphologies is plotted in Figure B.4 and shows the starting simulations all arriving at Janus-like morphologies suggesting equilibrium is reached.

To complement the SSR_{sim} an additional quantitative measure of the monolayer was created to characterize the NP monolayer domains. While SSR is a standard experimental measure for characterizing the degree of phase separation in NP monolayers, it provides an incomplete understanding of the type of phase separation. To provide a more descriptive measure of the monolayer morphology we measure the patch areas within the monolayer. To measure the patch size, we group the ME ligands into clusters. We considered any ME ligands separated by a distance less than 6Å to be within the same cluster. We group all ME ligands into clusters based on this criterion and characterize them by the how much of the NP surface area they cover. As a demonstration of the usefulness of this metric, we look at a Janus-like patchy particle from our simulation and compare it to a NP monolayer with 1nm stripes. These two NP monolayers map to nearly the same SSR even though these monolayers show different morphology. However, the largest ME cluster area of these two NP monolayers is significantly different as the circular patches have a greater area to circumference ratio. An example of this is shown in Figure B.5, here we compare a patchy particle with a striped particle with 1nm stripes. Though the striped and patchy particles show different morphologies the SSR values map to nearly the same value, however the area of the largest ME patches show significant difference due to the cluster shape in each monolayer. Taking this into consideration we also apply the largest cluster size analysis to the configurations used in our equilibration check. Comparing the initial and final largest ME patch area from all the configurations show a convergence (see Figure B.6) which again suggests that after 800k steps the simulation has reached equilibrium.

4.3 Results & Discussion

In this section, we begin with a discussion of our nanoparticle monolayer system, focusing on its components, synthesis, and characterization via TEM. Then we will discuss our computational model and sampling algorithm. From both approaches, we obtain distributions of 5-ligand fragment clusters and discuss the information they provide on the degree of phase separation in the NP monolayer. In the process, we explain the origin of an unexpectedly large variance in the experimental data. Finally, we make use of the atomistic structures that we've obtained to understand the monolayer morphology in greater detail.

Synthesis and TEM Characterization of Ultrasmall NPs with a DDT/ME Monolayer

Ultrasmall silver metal NPs were synthesized as described in our previous paper,56 with a dodecanethiol (DDT) and mercaptoethanol (ME) monolayer. We chose to focus on a mercaptoethanol (ME) and dodecanethiol (DDT) monolayer as these ligands differ both physically and chemically. Additionally, the expected hydrogen bonding between the ME alcohol functional groups as well as the crystallization among the DDT ligands [**?**] presented a good test system with a range of interactions that might be expected to drive bulk phase separation. The presence of these common NP monolayer intermolecular interactions afford us a chance to ensure that our computational model is sufficiently accurate to model their effects. The ratio of DDT to ME in the synthesis solution ranged from 50 : 50 to 80 : 20 in order to vary the ligand ratio on the nanoparticle surface. To ensure any excess reactants were removed after each synthesis the NP solution was centrifuged at 12000 RPM for 20 minutes. Following centrifugation, the supernatant was decanted and replaced with fresh ethanol. Subsequently the NPs were redispersed via sonication and again centrifuged. This wash process was repeated three times, and after the third and final centrifugation, the NPs were redispersed in toluene instead of ethanol. The NPs were imaged using TEM to determine the size distribution and general shape of the NPs. Ligand protected NPs appeared roughly spherical and ranged from $2 - 10$ nm in diameter, with a median diameter of 4 nm, an average diameter of 5nm, and a standard deviation of 2 nm (see Figure 4.1).

Simulations of Ultrasmall NPs with a DDT/ME Monolayer

For our computational work, we set up our simulations to include a realistically faceted NP (important for accurately modelling ligand crystallization), an accurate atomistic potential (important for accurately modelling hydrogen bonding and other enthalpic effects), and a configurationally biased sampling algorithm (important for equilibrating our system). In addition, to connect experiment and theory, we devised a method to analyze the resulting structures in a way that can be directly compared to experimental results. Our simulations took place on icosahedrally faceted NPs. We used an atomistic OPLS united

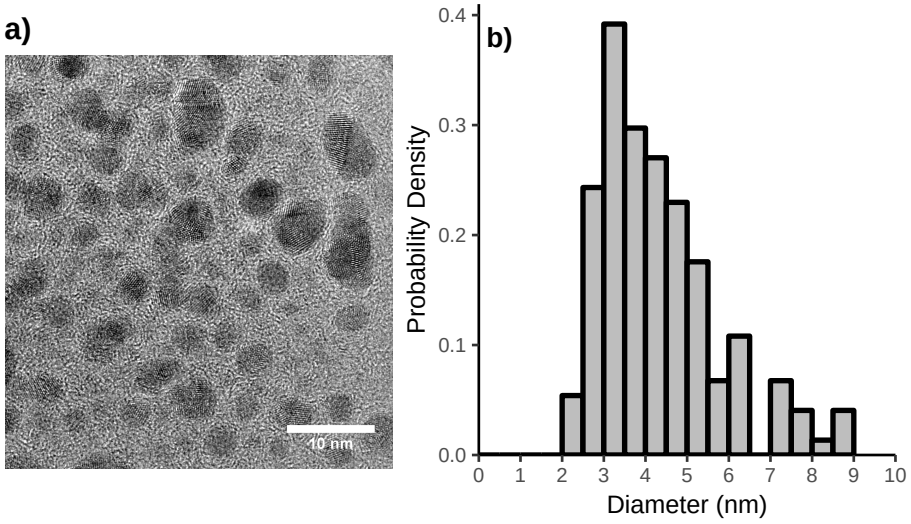

Figure 4.1: NP shapes and size distributions from TEM. (a) A representative TEM image of silver NPs with dodecanethiol (DDT) and mercaptoethanol (ME) monolayer. (b) Histogram of particle sizes derived from TEM measurements.

atom potential that appropriately represents the intermolecular interactions found in our system. Additionally, to overcome problems associated with the long time required for equilibration, we implemented a Monte Carlo method that utilizes unphysical moves to improve sampling by more easily bypassing large potential energy barriers. When modelling chain molecules, the potential number of self-avoiding walks grows rapidly with chain length, making it difficult to appropriately sample their conformations. The sampling difficulty is compounded within dense monolayers, since a significant fraction of the configuration space is unphysical due to chain overlaps. To combat this problem, our simulations included an unphysical move, first described by Siepmann et al., [106] that biases the selection process of chain configurations using Rosenbluth weights while maintaining detailed balance. [106] This configurationally biased Monte Carlo (CBMC) method has been used successfully to determine phase separation in multi-ligand monolayers on flat surfaces. [104, 107] More recently, it has been utilized to study monolayer phase separation on spherical gold nanoparticle for monolayers with physical mismatch. [103] Here, we extend the CBMC method to our physically and chemically mismatched system, enabling us to more efficiently approach equilibrium than we would be able to with comparable molecular dynamics simulations. This improved efficiency is even more vital, since the alkanethiol ligand monolayer has extremely slow kinetics-recent work by Luo et al. shows it can take up to 4 days for alkanethiol monolayers to reach equilibrium. [91]

Six simulations were run at 298K for each ratio of DDT/ME, all starting from a randomly mixed initial configuration. The number of steps, 800,000, was determined through several equilibration checks including a series of test simulations starting from a diverse set of initial monolayer morphologies including mixed, striped, and Janus (see Figures S3-S5 for more information). Additional simulation details are provided in the Methods section.

Experimental and Simulated MALDI-MS Results

The synthesized NPs were analyzed via MALDI-MS as described in our previous studies [38,87] to determine the actual ratios of DDT to ME on the NP surface for each sample as well as the degree of ordering in the corresponding thiolate monolayer. Performing MALDI measurements with thiolate monolayers on noble metal NPs produces characteristic fragments with a predictable ratio of thiolate ligands and metal atoms. For thiolate monolayers on silver metal NPs, the characteristic fragments follow the pattern $Ag_{n+1}L_n$ where L represents a thiolate ligand and n is an arbitrary integer. [26,50] As in our previous work, [38,87] we analyze the Ag_6L_5 fragments of the mass spectrum as they show the strongest signal to noise ratio in our spectrum. With two different thiol ligand types on the surface (ME and DDT), the Ag_6L_5 fragment type has six possible MS peaks, one for each of the following ligand combinations: 5 ME/0 DDT ligands, 4 ME/1 DDT ligands, 3 ME/2 DDT ligands, 2 ME/3 DDT ligands, 1 ME/4 DDT ligands, and 0 ME/5 DDT ligands. The left of Figure 4.2a shows a sample mass spectrum of these peaks where the mole fraction of DDT (χ_{DDT}) is equal to 0.60. If the ligands are randomly mixed within the monolayer, then it is expected that the relative frequencies of the Ag_6L_5 peaks will follow a binomial distribution. Therefore, a departure from the binomial distribution indicates a departure from a randomly mixed monolayer. To the right in Figure 4.2a we show both the binomial distribution (red) expected for a random monolayer as well as the experimentally determined distribution (black) from the mass spectrum shown on the left. We quantify the departure from the expected binomial distribution by taking the sum of the squared residuals (SSR) of each of the experimental peaks from the expected binomial distribution for the experimentally measured χ_{DDT}, as can be seen on the right in Figure 4.2a. Thus, the SSR quantifies the non-random nature of the nanoparticle monolayer, with an increasing SSR indicating an increasing amount of phase separation among the ligands in the monolayer.

The data obtained by the MALDI-MS experiments are then compared to results from the CBMC simulations run at five different values of χ_{DDT}, ranging from 0.20 to 0.80. To bridge the gap between our simulated and experimental data, we developed a technique to determine the expected MALDI-MS spectrum from the XYZ coordinates produced by the atomistic simulation, as outlined in Figure 4.2b. A single ligand was chosen at random from the NP, and its four closest nearest neighboring ligands (within $6\mathring{A}$ of the chosen ligand) were then selected to collectively represent a single 5-ligand fragment in the

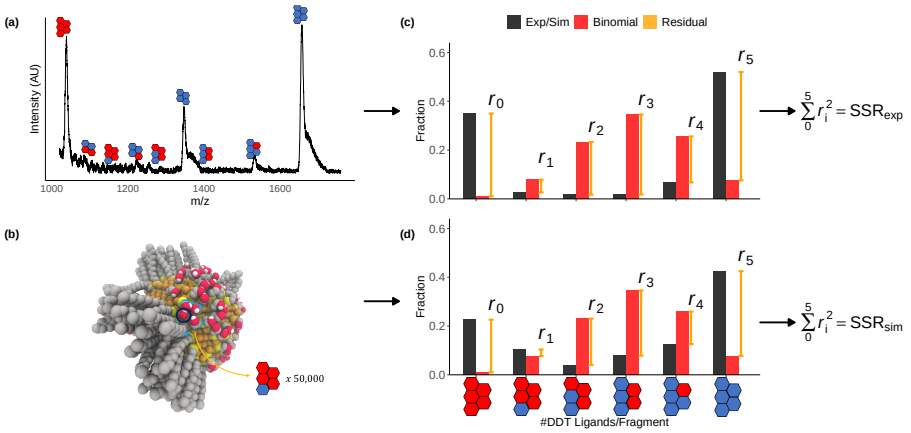

Figure 4.2: Diagram of the process for obtaining the MALDI-MS distribution for both the experimental and computational systems. (a) Representative raw MALDI-MS spectrum of a DDT/ME monolayer protected silver nanoparticle with . Ag6L5 fragment peaks are each represented by 5 hexagonal tiles, one for each ligand, with red hexagons representing ME ligands and blue hexagons representing DDT ligands. Ag5L4 fragment peaks are also marked in the spectrum as the three heaviest peaks of the Ag5L4 fragment type lie within the m/z range of the Ag6L5 fragment type. (b) Illustration of method to extract expected MALDI-MS distributions from the atomistic simulations. Here carbon is shown in gray, silver in orange, oxygen in red, hydrogen in white and sulfur in yellow. To build up these distributions, a ligand is selected at random (circled in dark blue), then four of the nearest neighbors are selected (highlighted in the dashed light blue line). The sampled fragment is then categorized by its DDT count and added to the count of the associated fragment type. The distributions for the experimental (c) and computational (d) results are normalized and compared to the binomial distribution for the corresponding ratio of DDT/ME ligands on the surface. A quantitative comparison is then made by comparing their respective SSR values.

MALDI-MS distribution. This procedure was then repeated 50,000 times to build up an expected fragment distribution for each simulated monolayer, as can be seen on the right in Figure 4.2b. From this distribution, we calculated an SSR_{sim} to quantify the difference between it and the expected binomial distribution.

To quantitatively relate the computationally and experimentally generated spectra, values of SSR_{exp} (black circles) and SSR_{sim} (grey triangles) are plotted in Figure 4.3a against the experimentally determined and input, respectively, χ_{DDT}. The SSR values from our simulations match well to the experimental values, giving confidence in the accuracy of the atomistic simulations. Examining both SSR values for the DDT/ME monolayers we find significantly higher values (average $SSR_{exp} = 0.32$ and average $SSR_{sim} = 0.28$) than in our previous work on physically mismatched monolayer mixtures, where the ligands differed only in carbon number (average $SSR_{exp} = 0.06$). [38] These high SSR

values when compared to the binomial distribution suggest a much greater degree of phase separation in the ME/DDT monolayers than in the physically mismatched monolayers in our previous work. [38,87] The higher range of SSR is in agreement with previous studies that suggest Janus-like monolayer phases correspond to SSR values greater than 0.1. [33,108] The consistently high value in the SSR data suggests that Janus-like phases are seen throughout the range of values. While the simulation data shows a good match with the mean values of the experimental data, there is a substantial spread within the experimental results. The large spread in the SSR_{exp} values, both experimental and simulation (SD=0.12, 0.07, respectively) is in line with previous work looking at highly phase separated monolayer protected noble metal NPs. [108] Further analysis of the SSR_{exp} spread is explored in the next section.

The calculated MALDI-MS distributions at 0.6 χ_{DDT} were also compared to an averaged representation of the experimental MALDI-MS distributions in Figure 4.3b. The MALDI-MS distribution shown in black in Figure 4.3b is composed of all experimental points within 0.01 χ_{DDT} of 0.60 χ_{DDT}, shown as the range bracketed in yellow in Figure 4.3a, while the MALDI-MS distribution shown in grey in Figure 4.3b is composed of the six simulations run at 0.60 χ_{DDT}. 0.60 χ_{DDT} was chosen here since the 0.60 ± 0.01 χ_{DDT} concentration range has the most experimental MALDI-MS measurements near a value explored in the simulation. In addition to the large number of MALDI-MS measurements at this point, the SSR_{exp} values in this range also display a large variance which is typical of the rest of the experimental data. The comparison in Figure 4.3b shows an excellent match between the experimental MALDI-MS distribution and the MALDI-MS distribution produced from the CBMC simulation. Both distributions show a Janus-like shape with large 0DDT/5ME and 5DDT/0ME peaks and much smaller intermediate peaks. A quantitative measure of the fit between these two distributions can also be obtained by taking the sum of the squared residuals between the experimental and computational MALDI-MS distributions. For the distributions shown in Figure 4.3b we obtain a $SSR_{exp\text{-}sim}$ value of 0.03 which is an order of magnitude smaller than the SSR_{exp} value between the experimental spectrum and the binomial spectrum of 0.33, and indicates an excellent correspondence between the experimental and simulation distributions. From these results it is clear that the DDT/ME nanoparticle monolayers are in a Janus-like phase across the tested range of surface concentrations.

Explanation of Large Variance in MALDI-MS SSR Values

The SSR values calculated for the DDT/ME monolayers show a larger spread, ($SSR_{exp} = 0.32 \pm 0.12$ and $SSR_{sim} = 0.28 \pm 0.07$) than in our previous dodecanethiol/butanethiol (DDT/BT) system ($SSR_{exp} = 0.06 \pm 0.04$). [38, 87] A higher variance in SSR values for ordered monolayers has also been seen in previous work by Iida et al., where a higher deviation in SSR values was reported for monolayers with SSR values greater than 0.1. [108] We hypoth-

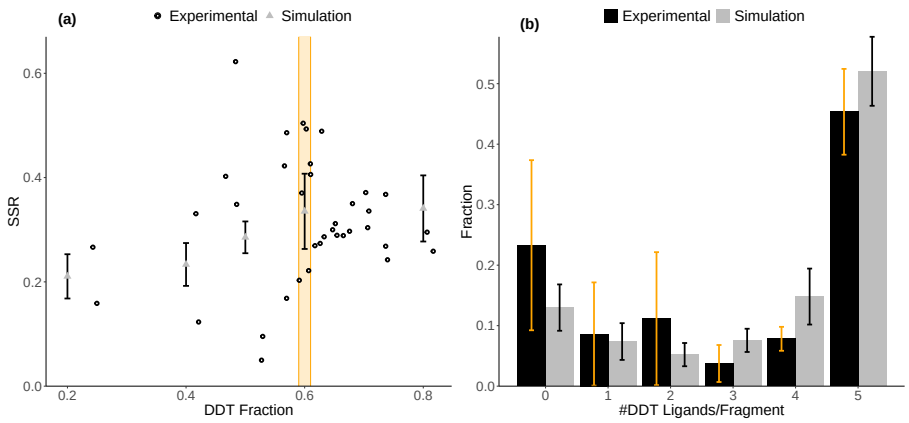

Figure 4.3: A comparison of experimental and simulated MALDI-MS results for ME/DDT monolayers. (a) The SSR values across a range of dodecanethiol fractions on the nanoparticle surface for both experimental results (open circles) and CBMC results (triangles). The error bars in the computational results are produced from the six simulations run at each point starting from different random configurations. (b) The MALDI-MS distribution, shown in black, was constructed from all seven experimental samples we measured that have a mole fraction of DDT of 0.60 ± 0.01 (enclosed by the orange shaded area). The calculated MALDI-MS distribution (shown in grey) was constructed from the six CBMC simulations run at χ_{DDT} 0.60.

esize that the increase in variance was due to two main effects. First, more highly ordered monolayers map to a larger range of SSR values than random monolayers, creating a large possible range of SSR values for relatively small fluctuations in well-ordered NP monolayers. Secondly, the variance observed in more highly ordered monolayers is magnified at lower nanoparticle diameters as each ligand represents a larger fraction of the total monolayer. To test these effects, we constructed a series of atomistic models of 0.50 monolayers for particles with diameters ranging from $2 - 6$nm. Janus monolayer models were simply constructed by randomly placing all DDT ligands on one half of the NP and all ME ligands on the other half. Random monolayer models were similarly constructed, but each ligand was randomly placed anywhere on the surface. For each combination of particle diameter and morphology, six such models were constructed. MALDI-MS distributions were then calculated for each of these constructed NP models, and their associated SSR_{sim} values are plotted in Figure 4.4. As expected, the results from the Janus monolayers show a much higher variance than those from the random monolayers. Additionally, smaller nanoparticle diameters Janus nanoparticles result in a lower expected SSR as well as higher variability in the expected SSR value. The variability in SSR_{sim} values for Janus-like monolayers in this exercise range from 0.16 to 0.62, which covers the majority of the variability seen in the experimental results in Figure 4.3a, where SSR_{exp} ranges from 0.06 to 0.62. Another potential

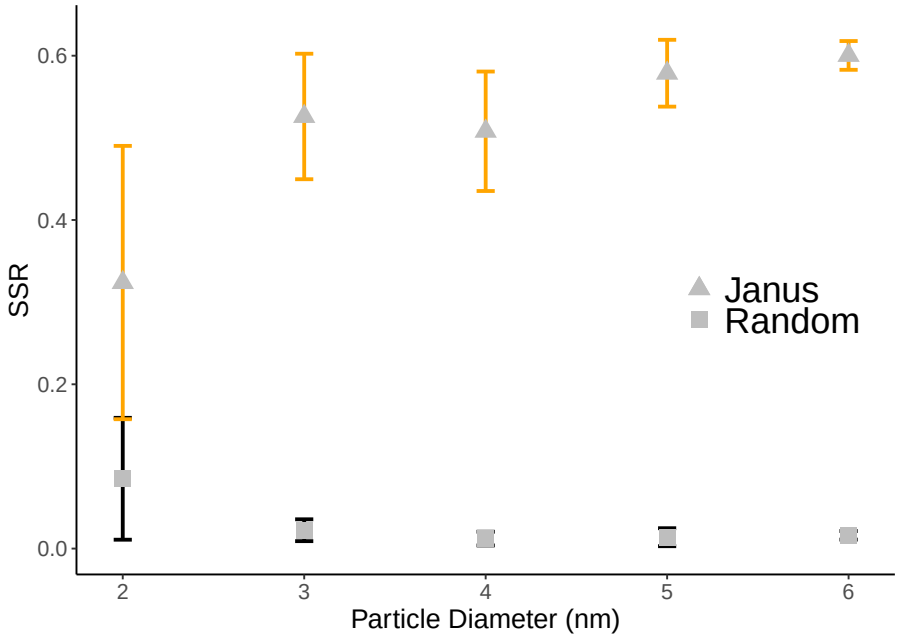

Figure 4.4: Analysis of sensitivity of SSR_{sim} in Janus and random monolayers at varying nanoparticle diameters. Here DDT and ME ligands are placed over the entire surface of the differently sized NPs either randomly (square points labeled "Random") or in separate hemispheres, creating Janus monolayers (triangle points labeled "Janus"). The SSR_{sim} is then calculated for each monolayer as outlined in Figure 4.2b. The square and triangle points are the average SSR_{sim} values for each particle diameter, and the error bars represent the standard deviations across the six trials conducted for each point.

factor in the SSR variance could be caused by the larger diameter particles forming stripy domains, as seen by Liu et al. [45] As seen in Figure B.4 these monolayers have a much lower variance contained within the SSR range of 2nm Janus NPs seen in Figure 4.4. Due to the lower variance of larger diameter striped NPs the effect on variance is expected to be minimal compared to that of Janus monolayers. Additionally, the transition in the observed monolayer morphology in Liu et al occurred between NPs of 2nm, which displayed a Janus morphology, and NPs of $4-5$nm, which displayed a striped morphology. As our simulated NP is 4nm in diameter and no striped phases are seen it is a strong indication that striped monolayers do not contribute to the majority of the experimental NP variance.

Analysis of Simulation Morphologies

More information about the underlying nature of the observed phase separation can be found by visually analyzing the atomistic structures of the

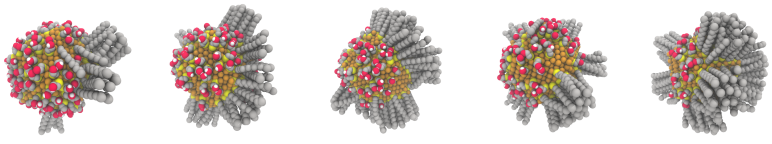

χ_{DDT}	0.2	0.4	0.5	0.6	0.8
SSR_{sim}	0.17	0.27	0.29	0.47	0.26

Figure 4.5: Representative monolayer morphologies from CBMC simulation at varying mole fraction of DDT from 0.2-0.8. The SSR_{sim} value of the structure shown is placed beneath each image in the last row. Carbon is shown in gray, silver in orange, oxygen in red, hydrogen in white and sulfur in yellow.

NP monolayer surface we obtained from our simulations. Figure 4.5 shows representative monolayers from the CBMC simulations spanning the range of DDT/ME ratios plotted in Figure 4.3a. Large, patchy, Janus-like domains can clearly be seen. This type of phase separation is consistent with previous simulation work which suggests that chemical mismatch induces patchy monolayer phase separation. [22, 34, 83, 88]

While SSR_{exp} is a standard experimental measure used to characterize the degree of phase separation in NP monolayers, it does not provide a complete picture of the monolayer morphology. To compliment the SSR_{exp} analysis, we also quantified the patchiness of the NP monolayers by measuring the area of the largest patch of ME ligands within each monolayer for all of our simulated structures. To do this we grouped all ME ligands separated by $6\mathring{A}$ or less into clusters. We then characterized those clusters by the fraction of the NP surface area they cover. The results are shown in Figure 4.6, where we can see that the largest ME patch for each χ_{ME} covers a proportional fraction of NP surface area. In addition, a large fraction of the NP surface area is covered by the largest ME patch, suggesting a Janus-like phase separation, and quantitatively confirming the visual interpretation of the computational monolayer snapshots in Figure 4.5 as well as the experimental MALDI-MS results.

Several physical forces are at play in the emergence of the observed Janus-like phase separation. First, the high energetic favorability of hydrogen bonding between ME ligands in the nanoparticle monolayer creates a large enthalpic incentive for clustering of ME ligands. Secondly, the Janus-like phase separation

is further favored by the clustering of DDT ligands, which is driven by crystallization of the longer DDT ligands. Crystallization of alkanethiols of similar chain lengths has been observed in previous simulation work on spherical and flat gold surfaces, [53,109] and can be seen in the structures shown in Figure 4.5. Because there is also a length mismatch between the two ligands, there is also an entropic driving factor which would drive the monolayer toward striped phases to maximize free volume of the longer ligands. [34] However, striped phases are not seen throughout the range of χ_{DDT} values. Indeed, simulations that start from a striped phase form Janus-like monolayers upon equilibration (see Figure B.4) suggesting that the chemical mismatch effects play a much larger role than the physical mismatch effects within this DDT/ME monolayer.

4.4 Conclusion

Using both the atomistic CBMC simulations and MALDI-MS experiments we have shown the ability to characterize the monolayer morphology of sub-10nm Janus-like NPs. Experimentally we find that our chemically and physically mismatched monolayer shows a higher degree of phase separation than the previously examined physically mismatched striped monolayers, [87] indicating the existence of large patchy domains. Computationally we find that the use of an atomistic simulation with a standard OPLS-UA force field and a CBMC algorithm to efficiently sample the relevant phase space provides an efficient method to arrive at the equilibrium monolayer structure. Using our method of deriving a MALDI-MS distribution from the atomistic simulations, we can make a direct quantitative comparison between the experimental MALDI-MS spectra and the atomistic simulations. This comparison shows good agreement, both when we compare fragment distributions and in terms of the trend across the range of χ_{DDT} values. This agreement gives us additional confidence in our computational results, which show a patchy, Janus-like morphology. The computational approach described here provides an efficient method for predicting the expected Janus-like phase separation in monolayers where both physical and chemical mismatch exists, since the more accurate atomistic potential can capture the effects of important intermolecular forces and the CBMC sampling can accelerate the simulation's approach towards equilibrium. We expect that it should prove similarly effective at predicting other ligand-shell morphologies, but additional work is needed to confirm its efficacy in those cases. Application of this technique may allow for a more rapid design of multi-ligand ultra-small NPs with specific monolayer morphologies for use in applications ranging from drug delivery to photonics.

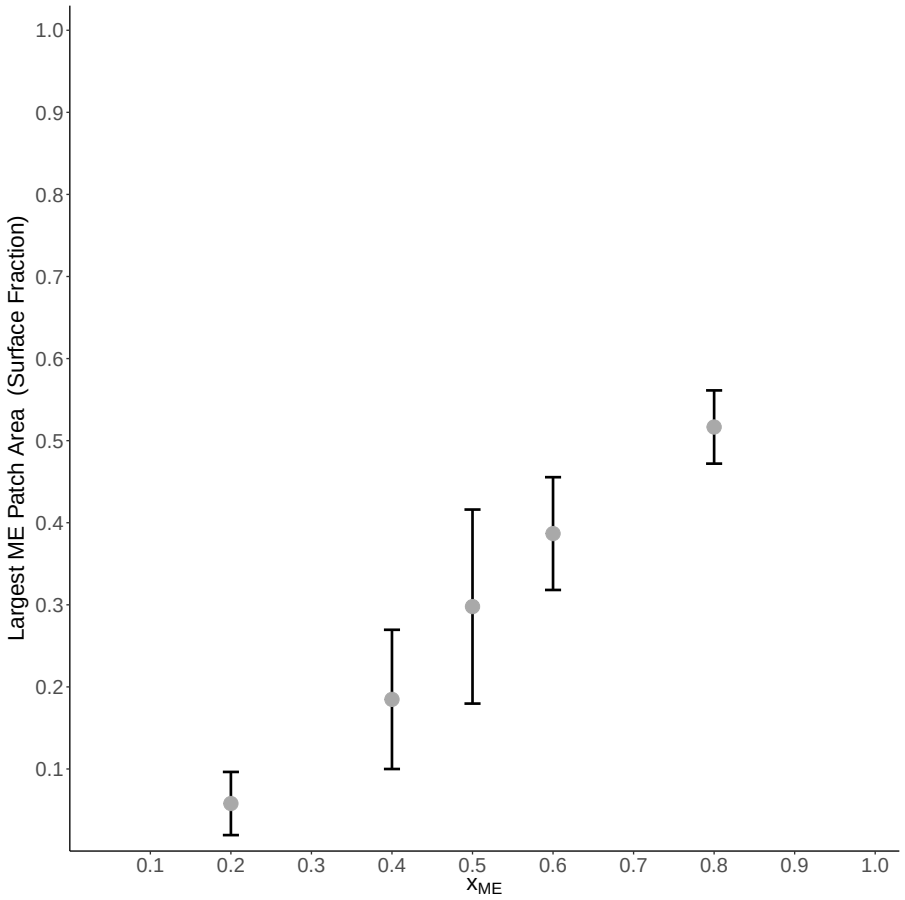

Figure 4.6: Analysis of the largest ME patch in each simulated NP monolayer. Surface area of the largest ME patch of each monolayer plotted as a function of ME surface fraction. The y-axis is in units of the fraction of total surface area of the NP surface. Final structures from all six simulations at each were used to calculate the averages and standard deviations plotted here.

Chapter 5

Predicting Phase Mismatch

Using CBMC simulations to predict trends in mercapto-alcohol/alkanethiol monolayers with varying chain length mismatch

This chapter was adapted from unpublished work by: Steven N. Merz, Elise Hoover, David Green, Kateri DuBay

5.1 Introduction

Multifunctional nanoparticle monolayers (NP-SAMs) from mixtures of alkanethiol ligands have a wide variety of applications from photonics [16,36,56–58] and catalysis [13, 110] to biological sensors [68, 69] and drug delivery [59–62]. As such the design and characterization of these monolayers has attracted a wide variety of interest [10, 111, 112]. The design of these MNPs is especially centered around designing SAMs on the NP surface that add functionality to the NP. This design is critical to MNP properties as the interfacial area of the MNP comprises a large percentage of the NP. These SAM monolayers can be enhanced with the use of multiple ligand types which can add multifunctional properties to the MNP [8, 10, 111, 113].

With the use of multiple ligand types many multi-ligand monolayers will undergo some type of phase separation [22, 112, 114], especially if these ligands include different functional groups. Several studies have shown that monolayer phase separation can have a significant impact on the properties of multifunctional nanoparticles [9, 10, 73, 82, 115] making controlling and understanding NP monolayer phase separation a key component to effectively designing multifunctional MNPs. To investigate this phenomenon several experimental studies have been done to investigate the underlying factors of NP monolayer phase separation [45, 46, 54, 71, 75, 112]. These experimental studies give clues to the degree and type of phase separation, but do not give a detailed picture of the monolayer morphology. As the nature of the phase separation detected by

indirect experimental methods additional work is needed to understand self-assembly in NP monolayers.

Previous studies have looked at modelling phase separation of NP monolayers using molecular simulations to assist in filling in this gap [23, 34, 53, 83, 90, 103, 116, 117]. These studies aid in revealing the detailed interplay between ligands that occurs during phase separation of multi-ligand monolayers. However, much of this work lacks direct comparison to experimental results. Without this direct comparison it is difficult to tell whether these simulations fully capture all the relevant details of NP monolayer phase separation. Some recent studies have made progress in comparing experimental and computational results. This includes work by Luo et al. [86] which looks at comparing SANS analysis of NP monolayers with DPD simulations. This method has a few drawbacks including the use of SANS which requires the use of a neutron source as well as selective deuteration of ligands which adds a higher level of complexity than most other experimental methods. Additionally, the use of DPD simulations to determine the equilibrium monolayer morphology can be problematic as the largest time scale that can be probed by DPD simulations is on the order of microseconds and the time scale of equilibration of thiol monolayers on noble metal nanoparticles can take up to 4 days [91].

Recently, we have shown the efficiency and simplicity of using molecular modeling in tandem with MALDI-MS to analyze NP-SAMs. MALDI-MS is a much more accessible technique than SANS only requiring a UV laser for ablation and a mass spectrometer. Our recent work with MALDI have shown the ability to detect phase separation in physically mismatched alkanethiol monolayers [38,87] as well as in a physically and chemically mismatched monolayers [118]. To gain a full picture of the monolayer morphology we also model the monolayer computationally. As noble metal nanoparticle thiol monolayers can take up to 4 days to equilibrate [91] we use simulations that can search phase space in unphysical manners allowing the bypass of large kinetic barriers in monolayer equilibration.

In this manuscript, we show the versatility of using atomistic simulation as a tool for predicting monolayer phase separation by using CBMC to predict the trends in ligand patterning for hydrophobic/hydrophilic monolayers with varying degrees of chain length and chemical mismatch. To this end, three combinations of ligand mixtures were chosen from alkanethiols and mercapto-alcohols to explore the interplay of differing carbon chain length and varying functional groups on monolayer self-assembly (see Figure 5.1). The three monolayers explored include two with chain length mismatch – dodecanethiol/mercapto-hexanol (DDT/MHA) and hexanethiol/mercapto-undecanol (HT/MUDA) as well as one with no chain length mismatch - dodecanethiol/mercapto-undecanol (DDT/MUDA). On the basis of the theoretical predictions, we synthesized Ag NPs with the same 50:50 monolayers for analysis with MALDI-MS, facilitating

comparisons between theoretically and experimentally-derived spectra, whose agreement engenders confidence in the predicted CBMC profiles of the self-assembled monolayers. The ability to predict phase separation of NP monolayers will allow facile design of multi-functional MPNs for a variety of applications including drug delivery.

5.2 Methods

In this work we use the atomistic CBMC simulation used in our previous work [118] which uses the OPLS-UA potential along with a CBMC sampling scheme. The atomistic OPLS-UA potential allows a much more accurate model of interatomic interactions than other coarse grained modelling attempts such as those using DPD [34,72,86,119]. This added accuracy aids in the modelling of the complex intermolecular interactions in chemically mismatched monolayers and showed excellent agreement with the chemically mismatched monolayer in our previous paper [118]. The CBMC sampling scheme is necessary to overcome the large kinetic barriers seen in thiol noble metal monolayers. Previous work by Stellacci et al. has shown that equilibration of these monolayers can take up to 4 days [91]. As standard molecular dynamics techniques can only probe up to microsecond time scales the enhanced sampling provided by CBMC allows a much more efficient approach to equilibrium.

The atomistic CBMC simulations can then be compared directly to experimental MALDI results, through the use of the statistical sampling technique used in our previous paper [118]. In this technique a random ligand is chosen from the NP monolayer then the four nearest neighbors within a 6Å cutoff are chosen to create an Ag_6L_5 fragment. After 50,000 fragments are sampled from the NP monolayer they are binned by the ratio of the two ligand types within each fragment (i.e. 0 Ligand A/5 Ligand B, 1 Ligand A/4 Ligand B, 2 Ligand A/3 Ligand B, 3 Ligand A/2 Ligand B, 4 Ligand A/1 Ligand B, and 5 Ligand A/0 Ligand B) and then normalized by the total amount of fragments in order to compare with the experimental spectrum.

The synthesis of the multi-ligand coated silver nanoparticles was carried out using the one-step synthesis outlined in our previous work [20]. This technique allows the synthesis of uniform noble metal nanoparticles with multi-ligand monolayers without the need for ligand exchange steps. This reduces possible complicating variables that these steps introduce. To characterize the degree of phase separation of the NPs monolayers we use MALDI-MS which has been used successfully for this purpose in our previous work [38,87]. In this technique the nanoparticle samples are co-crystallized with a matrix agent, in this case trans-2-[3-(4-tert-Butylphenyl)-2-methyl-2-propenylidene]malononitrile (DCTB), which allows facile ionization of the AgNPs using a soft UV laser. Once the AgNPs are ionized they are then fed through a time-of-flight mass spectrometer to quantify each ionized fragment by their mass to charge ratio.

In noble metal thiol monolayers these mass spectra contain characteristic fragment families with a specified ratio of metal to ligands in each fragment. In silver thiol MPNs the characteristic ratio is $n+1$ silver atoms to n ligands or $Ag_{n+1}L_n$. In our work we have found that the Ag_6L_5 fragment family has the highest signal to noise ratio and therefore is used for analysis in this study. As each ligand has two ligand types with two distinct masses the Ag_6L_5 fragment family consists of 6 peaks one for each possible ratio between ligand A and ligand B in the Ag_6L_5 fragment (i.e. 0 Ligand A/5 Ligand B, 1 Ligand A/4 Ligand B, 2 Ligand A/3 Ligand B, 3 Ligand A/2 Ligand B, 4 Ligand A/1 Ligand B, and 5 Ligand A/0 Ligand B). If these two ligands are randomly mixed on the surface they should each appear within a fragment with probability proportional to their surface concentration. This suggests that the frequency of any one of the six peaks of the Ag_6L_5 fragment family should follow a binomial distribution, $B(n = 5, p = x_A)$, where $n = 5$ is used as a 5 trial binomial distribution models each of the 5 ligands in the Ag_6L_5 fragment and $p = x_A$ models the probability that any of the 5 ligands will be ligand A (the heavier ligand). This has been confirmed through several works including our own showing that monolayers with ligands containing only isotopic differences produce characteristic fragment peaks that follow the binomial distribution very closely [33, 38]. Based on this observation we can determine the degree of phase separation of a NP monolayer by its deviation from this binomial distribution. To quantify this, we take the squared residual between each peak and the binomial distribution and sum them to find the sum of squared residuals (SSR). As the SSR measures the deviation from the binomial distribution the larger the SSR value the greater the deviation from a well-mixed monolayer. Both the normalized Ag_6L_5 MALDI distribution as well as the SSR can be directly compared to the computational results. As such we can quantitatively confirm the accuracy of the computational simulations predictions of the NP monolayer phase separation through direct comparison to experiment.

5.3 Results & Discussion

Three different combinations of monolayer ligands were chosen to explore the effect of chain length mismatch on chemically mismatched monolayers. As we previously explored self-assembly in an alkanethiol and mercapto-alcohol monolayer we now look at how varying degrees of physical mismatch affect this phase separation. By understanding the effects of physical mismatch in multi-functional monolayers it should be possible to create multi-functional monolayers with any type of phase separation through alteration of chain length. Here we explore the effect of changing chain length mismatch in alkanethiol monolayers by looking at three alkanethiol/mercapto-alcohol monolayers with different degrees of chain length mismatch. One monolayer with a longer mercapto-alcohol and a shorter alkanethiol (mercapto-undecanol and hexanethiol), another with a shorter mercapto-alcohol and longer alkanethiol (mercapto-hexanol and dodecanethiol), and finally one monolayer with an

equal length mercapto-alcohol and alkanethiol (mercapto-undecanol and dodecanethiol).

The equilibrium monolayer morphologies were predicted via an atomistic CBMC simulation used to great effect in modelling mercapto-ethanol/dodecanethiol AgNP monolayers in our previous work [118]. This simulation uses an atomistic OPLS united atom potential in concert with a configurationally biased Monte Carlo sampling of phase space. The use of an atomistic potential allows for capturing of subtle intermolecular interactions important in chemically mismatched monolayers such as hydrogen bonding [118]. The use of the CBMC sampling scheme allows for a more efficient sampling of phase space of dense ligand monolayers as configurationally biased sampling avoids the large degree of physically unfeasible phase states that come from chain overlaps [104, 106].

To make sure that simulations were converging to the equilibrium morphology each simulation was run at two different start points - randomly mixed monolayers and Janus monolayers. By running the simulation from two points with large degrees of separation in phase space we gain a higher confidence that the simulation has reached equilibrium if the both simulations reach the same final configuration. This in addition to the six replicates for each starting point give a good sampling of the possible phase space of the NP monolayers.

Each set of simulations were run for 800,000 (800k) steps in line with our previous work on alkanethiol/mercapto-alcohol monolayers [118]. After the simulations the SSR values for each of the simulations' ending states were calculated for both the simulations starting at randomly mixed monolayers as well as the simulations starting at a Janus configuration. The comparison between the final SSRs of the two types of simulations are then compared to determine convergence. The results of this comparison are shown in Figure C.1 and show good agreement between the Janus initialized and randomly initialized monolayers all lying within the standard error of each other indicating the simulation approaches equilibrium after 800k CBMC steps.

Once we have ensured that our simulations have reached equilibrium we can then analyze the results with confidence. The SSR of the computational results from the 6 random trials of the trial with chain length mismatch (DDT/MHA and HT/MUDA) shows a large patchy degree of phase separation. Both values are above 0.10 which previous work are indicative of patchy monolayers [108]. The DDT/MHA monolayer ($SSR_{avg} = 0.20$) showed a higher degree of phase separation than the HT/MUDA monolayer ($SSR_{avg} = 0.14$). This is can be accounted for by the fact that a driving factor in alkanethiol segregation and this is not seen for HT monolayers on noble metal nanoparticles at room temperature [53]. In the DDT/MHA monolayers the alkanethiol ligand (DDT) is long enough for alkanethiol crystallization to occur and as the larger driving factor in mercapto-alcohol segregation is hydrogen bonding the shorter length

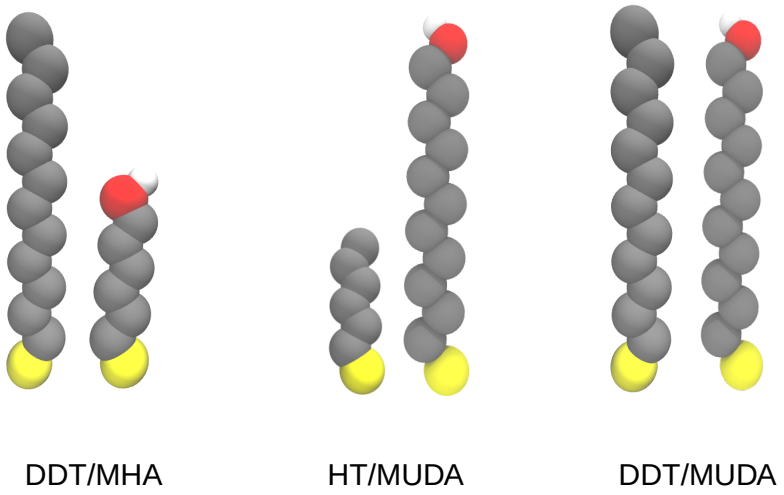

Figure 5.1: Diagram showing the three monolayer ligand systems chosen for this study.

of the MHA does not significantly hinder the segregation of the two ligands. However, the monolayer with no chain length mismatch shows little to no degree of phase separation. This seems to be due to the fact that the similar length ligands allow the mercapto-alcohols to incorporate into the alkanethiol crystallization process.

To confirm this prediction the simulated monolayer protected nanoparticles were synthesized experimentally. These silver nanoparticles were synthesized with the one-step synthesis process developed in our previous work [118]. This allows us to easy incorporation of multiple ligands into the nanoparticle monolayer without the use of multiple ligand exchange steps.

The synthesized particles were then analyzed using MALDI-MS using the same procedure as in our previous work [38,87,118]. This gives us a mass spectrum with characteristic fragment families with distinct ratio of silver atoms to monolayer ligands. For silver thiol monolayers this ratio is $Ag_{n+1}L_n$ in our case we analyze the Ag_6L_5 fragment family as this has the highest signal to noise ratio in our mass spectrum. After normalizing this spectrum and obtaining the SSR we obtain a direct quantitative comparison to the CBMC simulation predictions. In Figure 5.2 and Figure 5.3 we compare both the SSR values of the experimental and theory as well as their Ag_6L_5 MALDI distribution. For experimental MALDI results all spectra within 0.05 χ_{DDT} of 0.50 χ_{DDT} were included, while all simulations were run at precisely 0.50 χ_{DDT}. In all cases we show the CBMC simulations produce a good prediction of both the experimen-

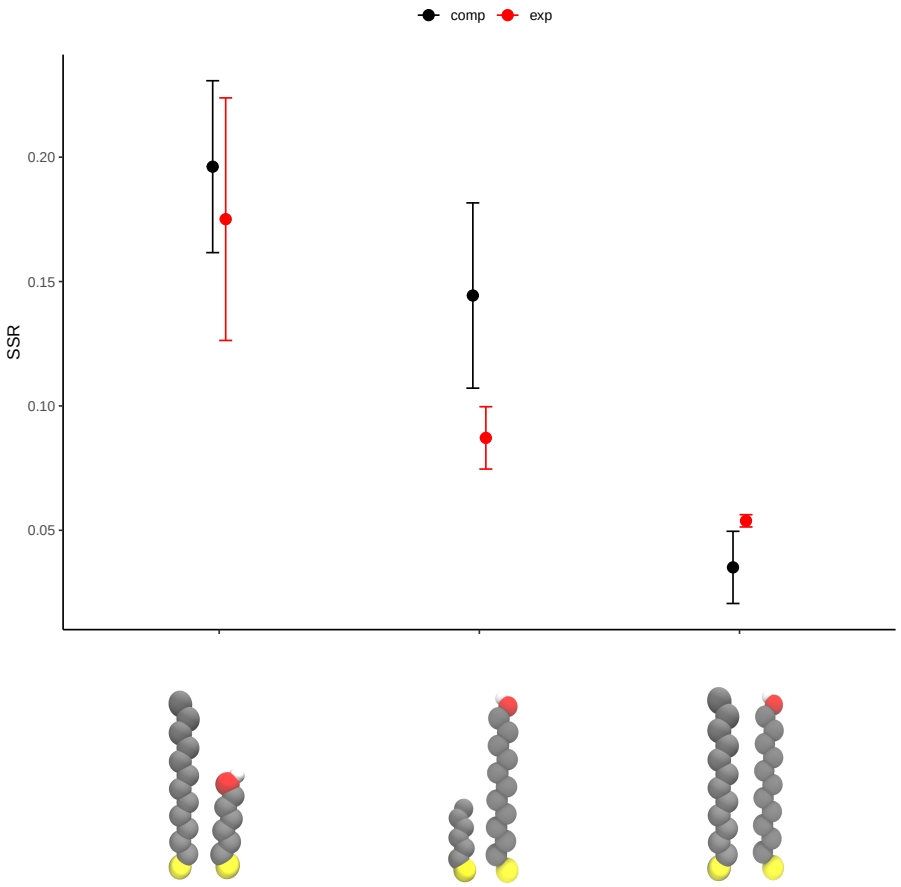

Figure 5.2: Comparison of simulation derived SSR values with the computational values

tal SSR as well as the experimental MALDI distribution, especially considering the wider variance of χ_{DDT} in the experimental spectrum.

In addition to predicting experimental results, the CBMC simulation can also provide additional information on the nanoparticle monolayer including the size of the patchy phases on the surfaces and detailed visualization of the monolayer morphology. While the experimental MALDI gives us an approximate measure of the NP monolayer's departure from a well-mixed monolayer through SSR, this provides little information on the detailed morphology of the NP monolayer. To gain further insight into the NP monolayer morphology we analyze the simulation results. Examining the atomistic CBMC simulations we see more clearly that the NP monolayers with chain length mismatch show large patchy morphology. Looking at the HT/MUDA monolayer we see

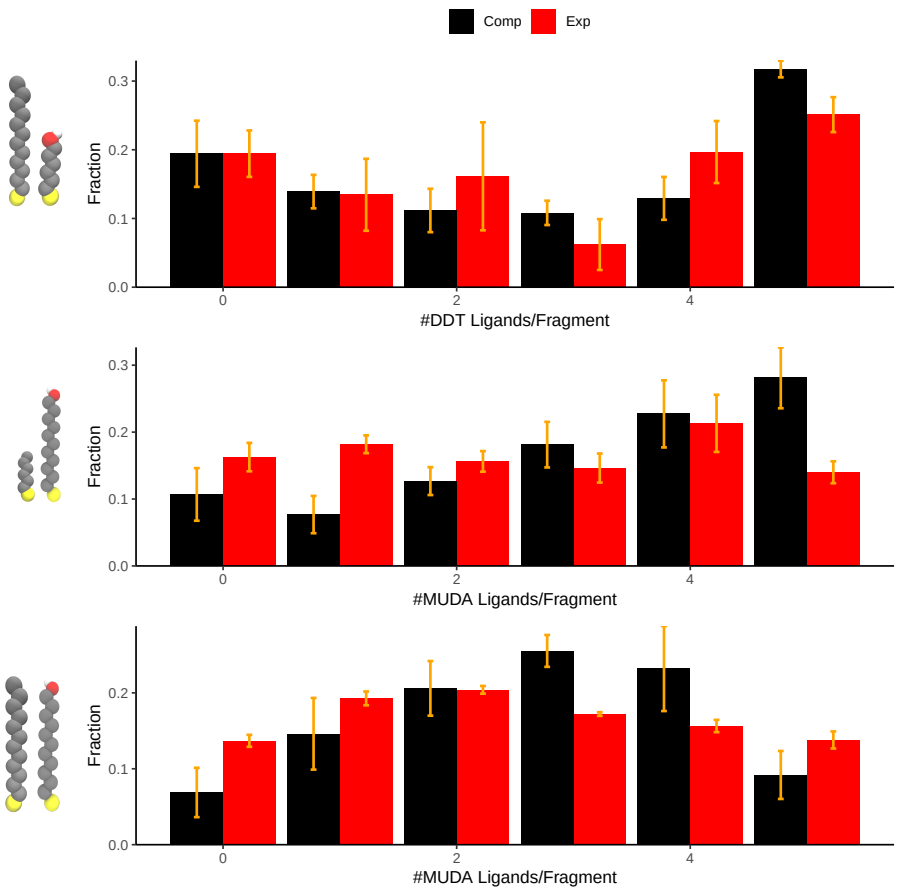

Figure 5.3: Comparison of experimental MALDI-MS spectrum with computationally predicted MALDI-MS spectrum

that while MUDA ligands show tightly clustered and segregated patches the HT ligands show little to no organization as the HT ligands are too short for crystallization to be favored at this temperature [53].

We can more quantitatively describe the monolayer morphology by quantifying the area of the largest hydrophilic patch in the NP monolayer. This trend is shown below in Figure 5.5 where the maximum patch area for each NP monolayer ligand system is quantified as the area of the largest mercapto-alcohol patch. A patch is considered to consist of all ligands within 6AA of each other, the total area is calculated as the half the area of the convex hull that contains the ligands sulfur atoms and is normalized by the total surface area of the NP. The trend in patch sizes follows a similar trend to the SSR values of the mono-

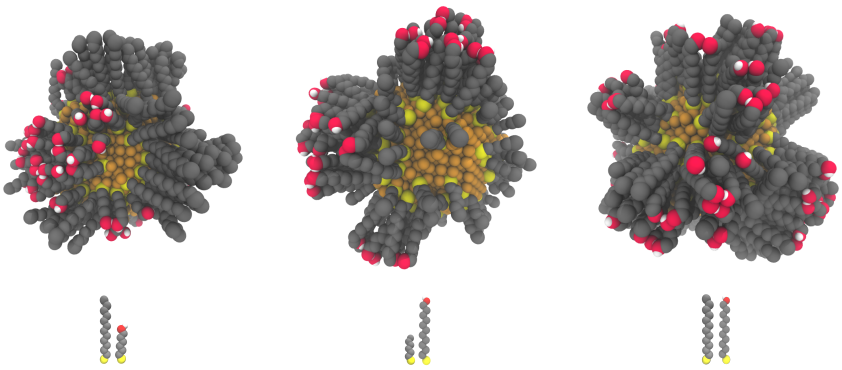

Figure 5.4: Snapshots of final configurations for each of the three simulations.

layers with the DDT/MUDA monolayer showing the smallest maximum patch sizes and DDT/MHA showing the largest maximum hydrophilic patches. It is interesting to note, however, that the maximum patch size of the HT/MUDA monolayer does not deviate as significantly from the maximum patch size of the DDT/MHA as the SSR values do. This also points to the fact that while the mercapto-alcohol ligands in both monolayers have a sufficient enthalpic driving force for segregation in hydrogen bonding the lack of an enthalpic driving force in the alkanethiol ligands in HT/MUDA monolayers is what causes the reduced degree of phase separation in HT/MUDA monolayers.

We can more quantitatively describe the monolayer morphology by quantifying the area of the largest hydrophilic patch in the NP monolayer. This trend is shown below in Figure 5.5 where the maximum patch area for each NP monolayer ligand system is quantified as the area of the largest mercapto-alcohol patch. A patch is considered to consist of all ligands within 6AA of each other, the total area is calculated as the half the area of the convex hull that contains the ligands sulfur atoms and is normalized by the total surface area of the NP. The trend in patch sizes follows a similar trend to the SSR values of the monolayers with the DDT/MUDA monolayer showing the smallest maximum patch sizes and DDT/MHA showing the largest maximum hydrophilic patches. It is interesting to note, however, that the maximum patch size of the HT/MUDA monolayer does not deviate as significantly from the maximum patch size of the DDT/MHA as the SSR values do. This also points to the fact that while the mercapto-alcohol ligands in both monolayers have a sufficient enthalpic driving force for segregation in hydrogen bonding the lack of an enthalpic driving force in the alkanethiol ligands in HT/MUDA monolayers is what causes the reduced degree of phase separation in HT/MUDA monolayers.

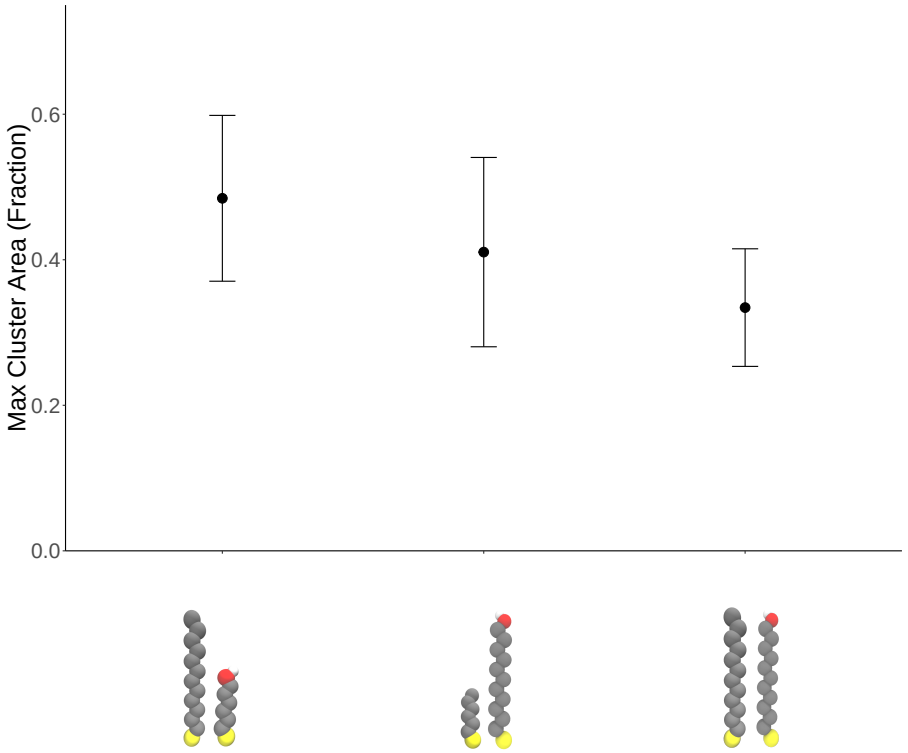

Figure 5.5: Maximum patch size for each multi-ligand monolayer predicted by CBMC simulations.

5.4 Conclusions

Our work demonstrates the ability for CBMC simulations to predict monolayer phase separation of alkanethiol and mercapto-alcohol monolayers. Our predictions shed light on the interactions of length and chemical mismatch on nanoparticle monolayer phase separation that cannot be observed through experimental techniques alone. Our analysis shows that while mercapto-alcohol ligands can show strong segregation through a wide range of chain lengths, alkanethiol monolayers need longer chain lengths for segregation. Additionally, we see that when the mercapto-alcohol and alkanethiol ligands have the same chain length the mercapto-alcohol start to integrate into the alkanethiol crystal structure drastically reducing segregation of the two ligands producing well-mixed monolayers. This allows the prediction and design of nanoparticle monolayers for a variety of purposes including drug delivery, bioimaging, and biosensing.

Chapter 6

Conclusion

6.1 Summary

In this work we have taken large strides in developing a simple and efficient method for characterizing ultrasmall (< 10nm) monolayer protected nanoparticles. These monolayer protected nanoparticles have a wide variety of applications including uses in optics [16, 36, 56–58], self-assembly [120], drug delivery [59–62], and biosensing [68, 69]. The ability to characterize and predict the phase separation of these NP monolayers will allow facile design of MPNs with multi-functional monolayers with increased drug delivery [9, 59, 75, 77] and unique self-assembled structures [120]. With the addition of this research, future work designing multi-functional can be sped along with the aid of predictive computational work and fast and efficient MALDI-MS validation.

Previous work with traditional techniques such as STM proved insufficient for characterizing small NP monolayers [40–43]. Several indirect experimental techniques have been used to characterize these ultrasmall NP monolayers [54, 82, 83]. But the interpretation of the results of these indirect experimental techniques has led to some debate [40–43]. Our work fills in this gap by weaving together simulation and experiment to create a characterization method that provides experimentally validated detailed information on NP monolayer morphology.

We take the simple and robust experimental technique of MALDI-MS along with computationally efficient techniques to create a new method for NP characterization which gives a detailed look at monolayer morphology through simulation with experimental validation. Previous work by Harkness et al. showed the potential of MALDI-MS for characterization of NP monolayers, but did not provide a direct link between the MALDI-MS distribution and detailed monolayer morphology. We fill in this gap through the use of computationally efficient SCFT simulations. We confirm the validity of this technique using a

control monolayer with only isotopic techniques along with a physically mismatched monolayer which we expect to show phase separation. The match between our hypothesis with experimental MALDI-MS and SCFT results validate our method and gives rise to a more robust method of characterizing noble metal nanoparticles.

With our method validated, we used MALDI-MS and SCFT to look at phase separation in monolayers with a range of physical mismatch to determine the relationship between physical mismatch and NP monolayer phase separation. By examining monolayers with alkanethiol ligands ranging from C4-C12 coadsorped with dodecanethiol, we were able to accurately model monolayers with a range of physical mismatch. By combining the experimental characterization of MALDI-MS with the insight provided by computational simulations we developed confidence in previous hypotheses about phase separation in physically mismatched monolayers.

We extend our work to modelling monolayers with Janus-like monolayers by studying monolayers that include a chemical mismatch. The extension of our previous modelling work is necessary in order to be capable of characterizing the full range of monolayer phase separations. With the added complexity of a chemical mismatch we found SCFT unable to accurately model the intermolecular interactions involved in chemically mismatched monolayers. Through the use of atomistic simulations with a CBMC sampling of phase space, we were able to use a detailed atomistic simulation that still efficiently converges to the equilibrium monolayer morphology. Comparison with MALDI-MS again validates our success, demonstrating that our method has the capability of modelling both chemically and physically mismatched monolayers.

We then tested the predictive power of our method with three different NP monolayers containing both physical and chemical mismatch. Simulations designed to predict the monolayer morphology of each of the three monolayer systems (DDT/MHA, MUDA/HT, and DDT/MUDA) were run before any synthesis work was performed. Results from these simulations coincided remarkably well with the experimental MALDI-MS results, confirming the predictive power of these simulations. The predictive power shown in this work lays the ground work for the computational design of multi-functional, monolayer protected NPs for a wide variety of uses including biosensing and drug delivery.

6.2 Future Work

With the validation of the predictive power of our method, there are several directions for future work. A simulation with predictive power would be useful for designing a wide array of monolayer protected NPs for a variety of applications. While the completed work has produced a simulation that can design

and predict an extensive variety of NP monolayers, extensions to this simulation could increase the applications of the simulation by modelling monolayers with more exotic functionalities.

One possible extension of our current work would be to increase our simulation to cover monolayers with a wider variety of functional groups, including amine and carbozylic acid head groups. These functional groups will bring in their own unique functionalities, which can broaden the array of self-assembled structures as well as their potential applications. Additionally these functional groups allow for facile bioconjugation of larger ligands as well as drug payloads that could increase their usefulness. The incorporation of these functional groups should be possible with the current OPLS-UA potential, however validation with experimental MALDI will take more time. Additionally, branched functional groups such as carboxylic acids will need a CBMC sampling that accounts for branching within ligands.

To extend the utility of our design method for nanoparticles in drug delivery, it is also possible to integrate cell membrane translocation simulations to predict ease of drug delivery for various monolayer phases. By coarse graining the predicted NP monolayer morphologies to a simpler DPD force field, it would also be possible to model the translocation with the aid of a metadynamic technique such as umbrella sampling. This technique aids in sampling the phase space of processes such as cell membrane translocation that have large kinetice barriers. These simulations will provide the free energy of each monolayer morphology alongside the morphology information given by the atomistic CBMC simulations. The added information provided by these metadynamic DPD simulations will allow for a streamlined pipeline for desigining MPNs for drug delivery applications.

Appendix A

Exploring Stripey Monolayers

A.1 TEM Images of Mixed Thiol-ligand Nanoparticles

In addition to the four TEM images shown in the main chapter, we collected TEM images for each of the other ligand systems. In Figure A.1 below are reproduced the TEM images for the dodecanethiol/pentanethiol, dodecanethiol/hexanethiol, dodecanethiol/heptanethiol, dodecanethiol/nonanethiol, dodecanethiol/decanethiol, and dodecanethiol/undecanethiol systems.

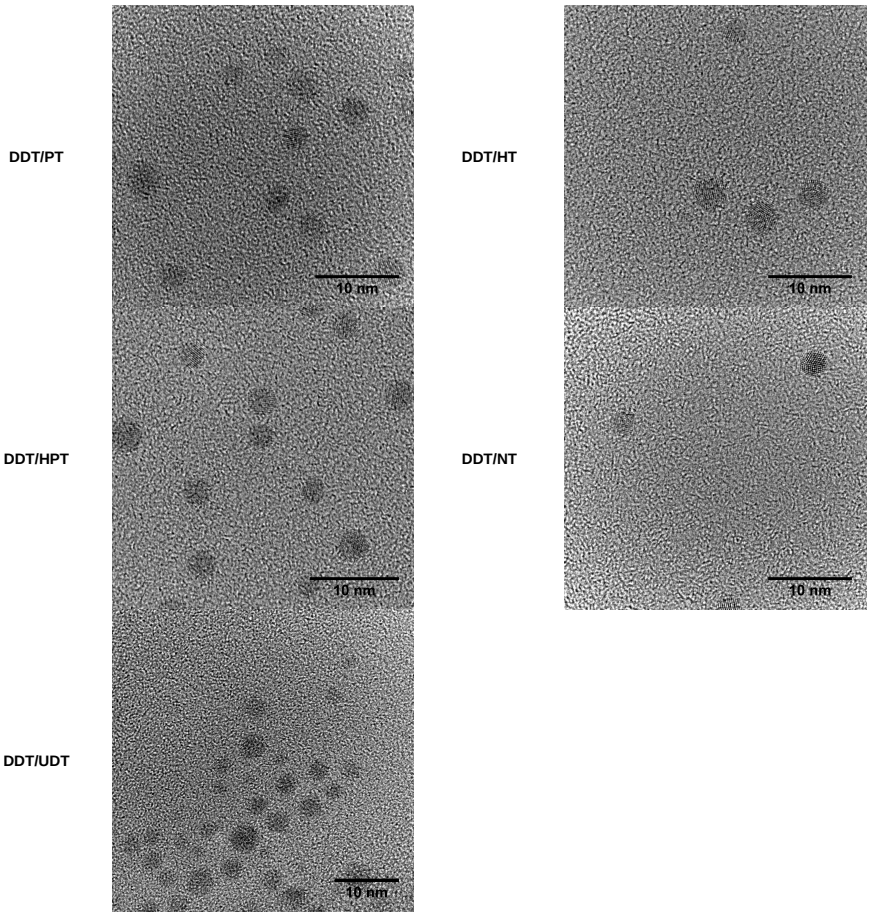

Figure A.1: TEM Images of Mixed Thiol-ligand Nanoparticles (DDT/PT) TEM image of dodecanethiol/pentanethiol functionalized nanoparticles. The measured sum of squares error for this sample was SSR= 0.0840, with a dodecanethiol surface mole fraction of χ_{DDT}= 0.52. (DDT/HT) TEM image of dodecanethiol/hexanethiol functionalized nanoparticles. The measured sum of squares error for this sample was SSR= 0.0215, with a dodecanethiol surface mole fraction of χ_{DDT}= 0.46. (DDT/HPT) TEM image of dodecanethiol/heptanethiol functionalized nanoparticles. The measured sum of squares error for this sample was SSR= 0.0076, with a dodecanethiol surface mole fraction of χ_{DDT}= 0.46. (DDT/NT) TEM image of dodecanethiol/nonanethiol functionalized nanoparticles. The measured sum of squares error for this sample was SSR= 0.0077, with a dodecanethiol surface mole fraction of χ_{DDT}= 0.44 (DDT/UDT) TEM image of dodecanethiol/undecanethiol functionalized nanoparticles. The measured sum of squares error for this sample was SSR= 0.0043, with a dodecanethiol surface mole fraction of χ_{DDT}= 0.55.

Appendix B

Exploring Patchy Monolayers

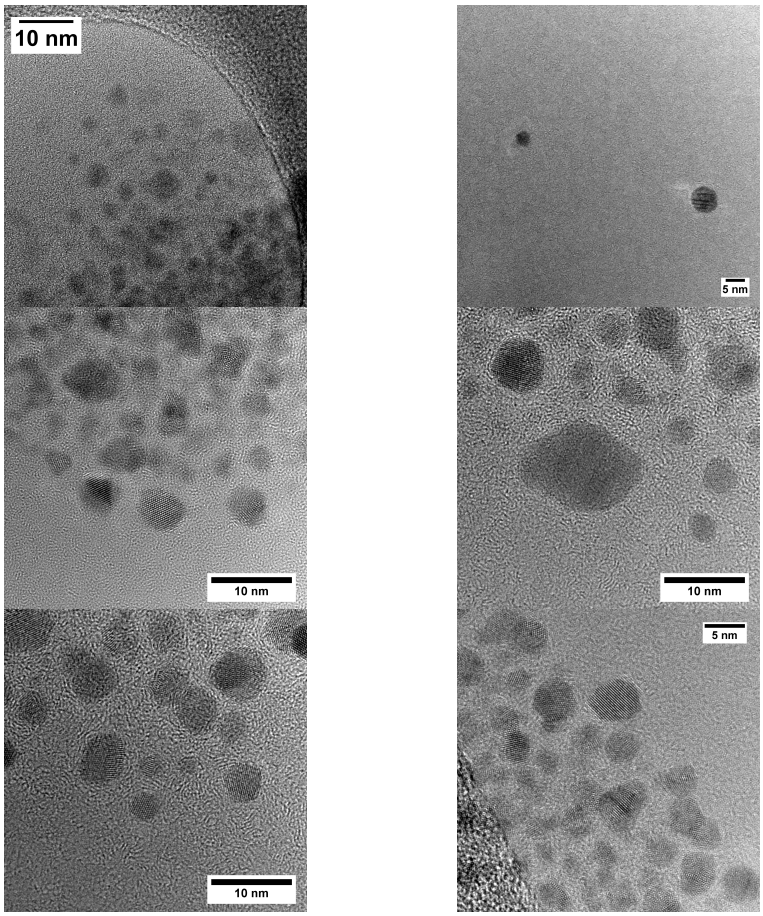

Figure B.1: Representative TEM images taken of DDT/ME monolayer silver metal NPs.

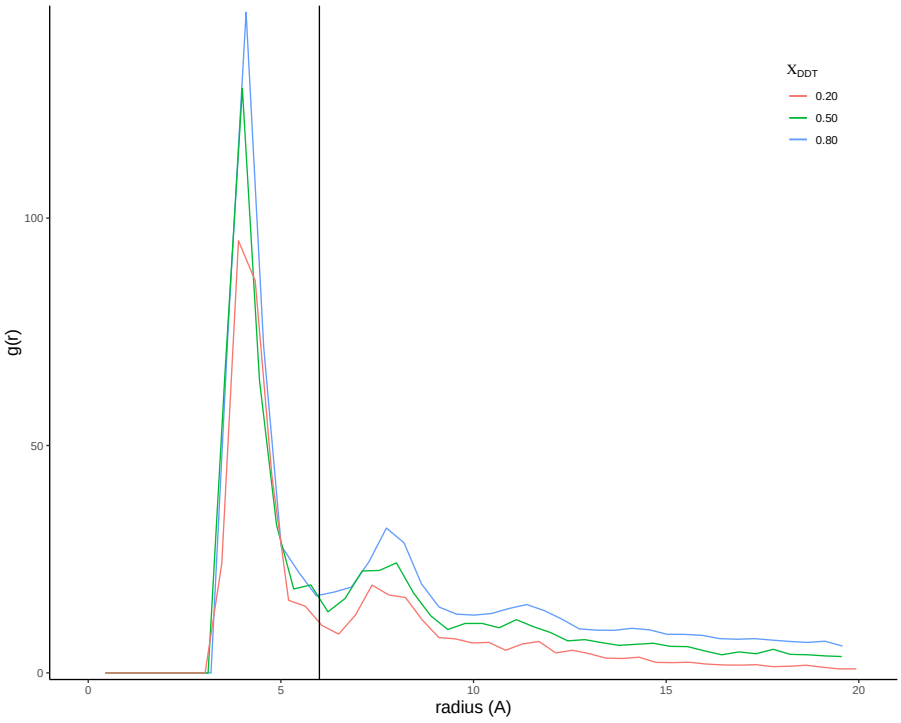

Figure B.2: RDF of DDT sulfur atoms at varying surface concentration of DDT on the surface. The first peak of the RDF shows the average distance between the sulfur atoms of DDT ligands to lie between $4 - 6$Å. A vertical line is placed at 6Å to illustrate the fact that 6Å lies at the trough between the first and second RDF peak making it a good cutoff for the nearest neighbor distance between ligands.

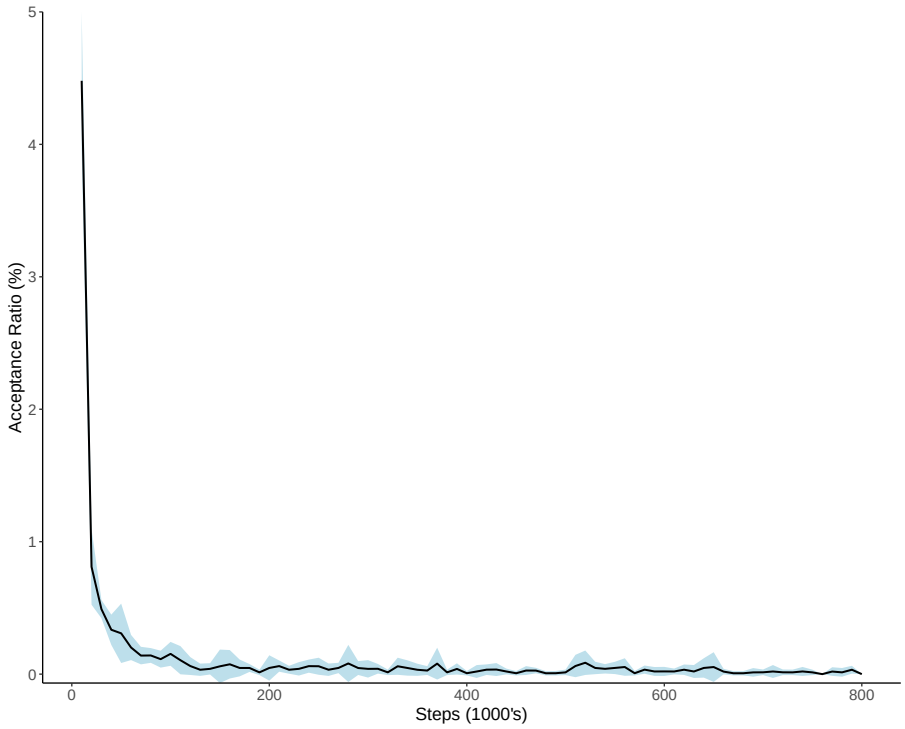

Figure B.3: Acceptance ratio of identity swap move over six trials of CBMC simulation at 0.50 χ_{DDT}. Blue ribbon shows standard deviation over the six trials and the average acceptance ratio, calculated every 10000 steps, is shown with the black line.

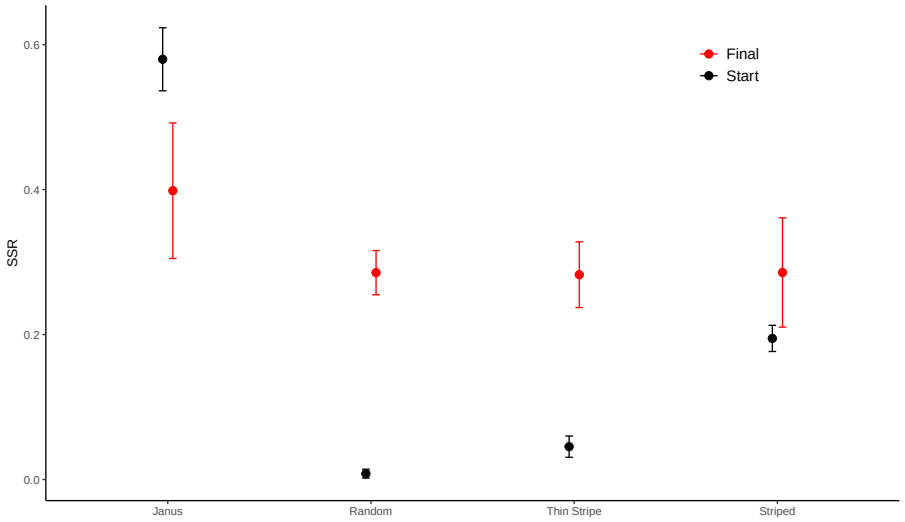

Figure B.4: SSR comparison between simulations with varying initial starting morphologies including Janus, random, thin 0.5nm stripes (Thin Stripe), and thicker 1nm stripes (Striped) for CBMC simulations run for 800k steps. The initial SSRs are shown in black circles while the SSRs of the final configuration are shown in red circles. Error bars represent standard deviation of the six simulations run for each data point.

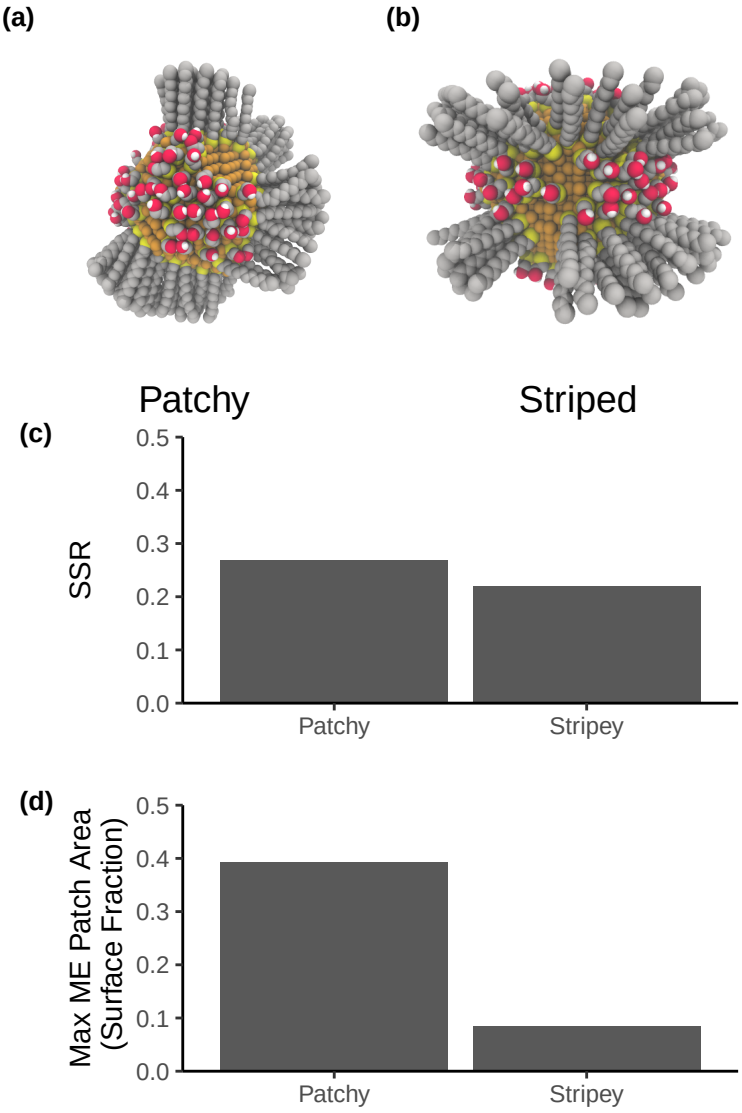

Figure B.5: Comparison of the two quantitative characterization techniques used for our nanoparticle monolayers SSR and max cluster area. (a-b) Example configurations of a striped and patchy monolayers. The striped monolayer is generated by constricting ligands within 1nm stripes and the patchy monolayer is the result of an 800k CBMC simulation at 298K, both monolayers contain a 50/50 ratio of DDT and ME. (c) SSR_{sim} values derived from the calculated MALDI-MS distribution for the patchy and striped monolayers shown in figures a and b respectively. (d) The area of the largest ME ligand patch on the surface normalized by the total surface area of the NP for the patchy and striped monolayers shown in figures a and b respectively

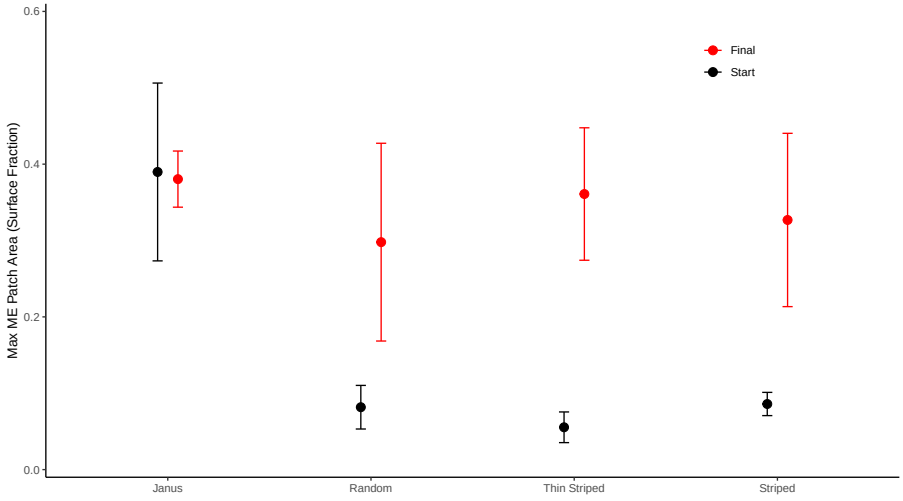

Figure B.6: Comparison of largest ME patch area of simulations with varying initial monolayer morphologies. Janus, random, 0.5nm thick striped, and 1nm thick striped monolayers are used as starting configurations for CBMC simulations run for 800k steps. Error bars represent standard deviation of the six simulations run for each data point.

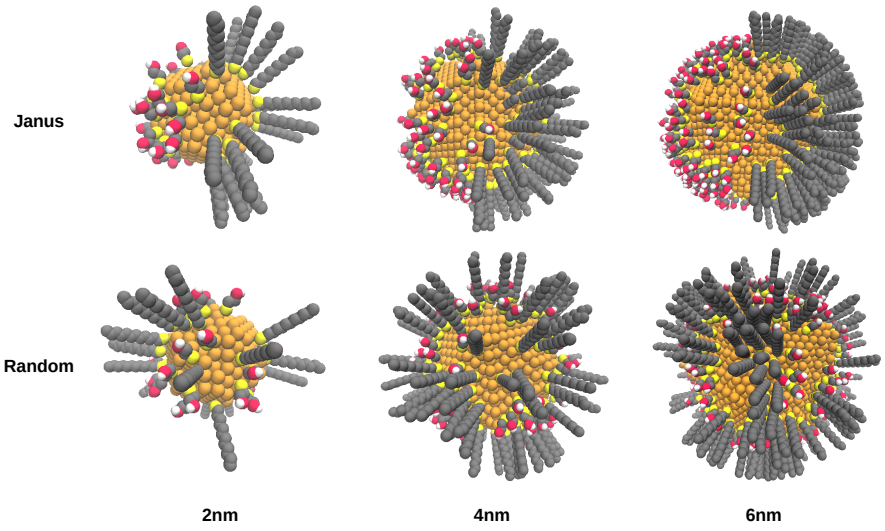

Figure B.7: Representative monolayers used for the SSR sensitivity analysis. The monolayers shown are for the 2nm, 4nm, and 6nm diameter particles. For Janus monolayer morphologies, the ME ligands were placed randomly within one hemisphere while the DDT ligands were placed randomly within the other hemisphere (top row). For random monolayers, both ME and DDT ligands are placed randomly across the entire NP surface (bottom row).

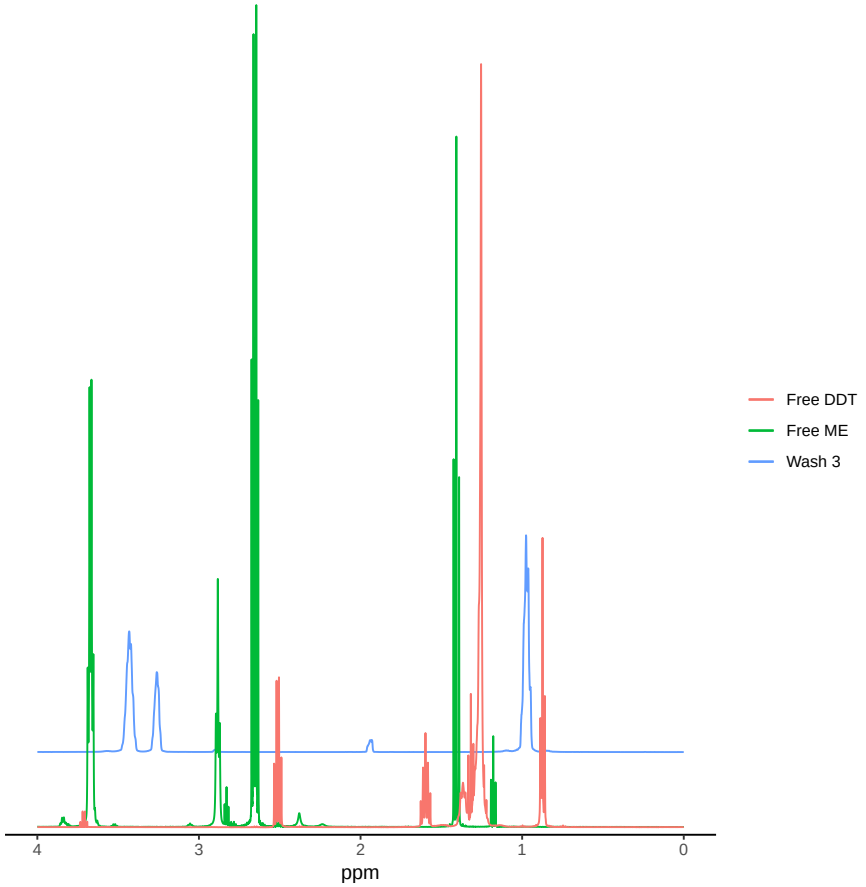

Figure B.8: 1H NMR of free thiol ligands along with a batch of silver DDT/ME nanoparticles after the three washes with ethanol used in our method. All samples were measured in 600μL of deuterated chloroform. After three washes the 1H NMR spectrum shows no sharp peaks indicating all ligands are bound to the noble metal nanoparticle surface.

Appendix C

Predicting Phase Mismatch

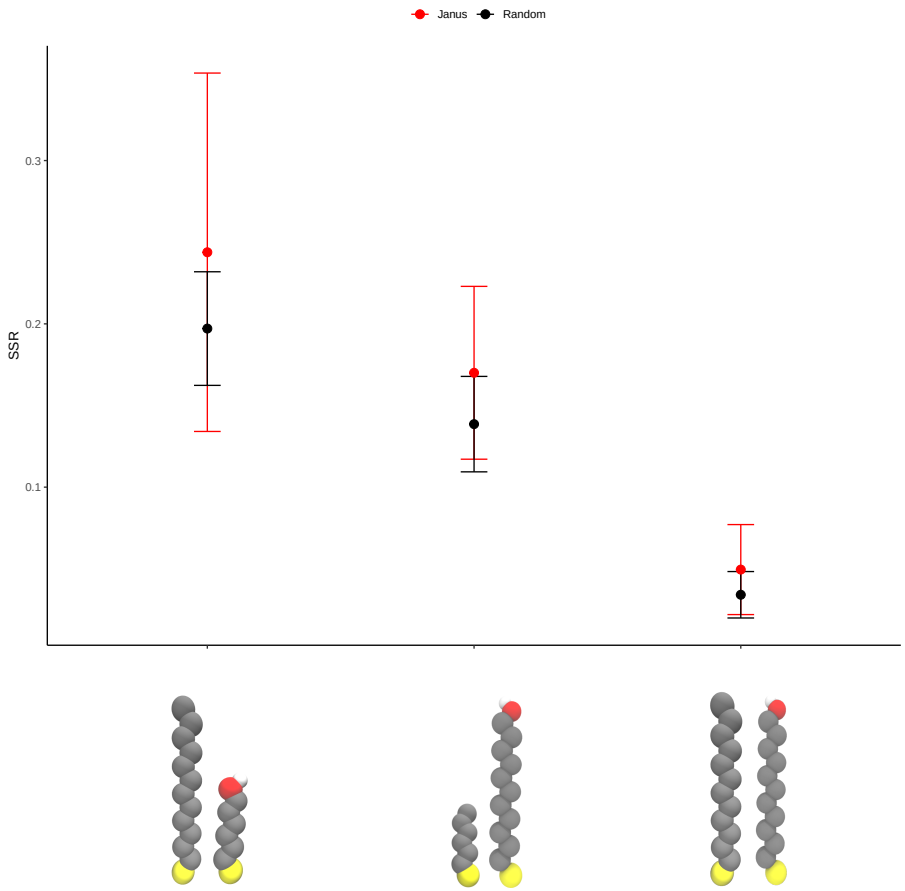

Figure C.1: Plot of convergence of SSR values for simulations started from Janus and randomly mixed monolayers.

Bibliography

[1] Eun Hye Jeong, Giyoung Jung, Cheol Am Hong, and Hyukjin Lee. Gold nanoparticle (AuNP)-based drug delivery and molecular imaging for biomedical applications. *Archives of pharmacal research*, 37(1):53–9, jan 2014.

[2] Rajib Ghosh Chaudhuri and Santanu Paria. Core/Shell Nanoparticles: Classes, Properties, Synthesis Mechanisms, Characterization, and Applications. *Chemical Reviews*, 112(4):2373–2433, apr 2012.

[3] Wafa' T Al-Jamal and Kostas Kostarelos. Liposomenanoparticle hybrids for multimodal diagnostic and therapeutic applications. *Nanomedicine*, 2(1):85–98, feb 2007.

[4] Allen C. Templeton, W. Peter Wuelfing, and Royce W. Murray. Monolayer-Protected Cluster Molecules. *Accounts of Chemical Research*, 33(1):27–36, jan 2000.

[5] Elodie Boisselier, Lionel Salmon, Jaime Ruiz, and Didier Astruc. How to very efficiently functionalize gold nanoparticles by click chemistry. *Chemical Communications*, (44):5788, 2008.

[6] Jennifer L Brennan, Nikos S. Hatzakis, T Robert Tshikhudo, Valdemaras Razumas, Shamkant Patkar, Jesper Vind, Allan Svendsen, Roeland J M Nolte, Alan E Rowan, and Mathias Brust. Bionanoconjugation via Click Chemistry: The Creation of Functional Hybrids of Lipases and Gold Nanoparticles. *Bioconjugate Chemistry*, 17(6):1373–1375, nov 2006.

[7] Gang Bao, Samir Mitragotri, and Sheng Tong. Multifunctional Nanoparticles for Drug Delivery and Molecular Imaging. *Annual Review of Biomedical Engineering*, 15(1):253–282, jul 2013.

[8] Chae-kyu Kim, Partha Ghosh, and Vincent M. Rotello. Multimodal drug delivery using gold nanoparticles. *Nanoscale*, 1(1):61, 2009.

[9] Ayush Verma, Oktay Uzun, Yuhua Hu, Ying Hu, Hee-Sun Han, Nicki Watson, Suelin Chen, Darrell J Irvine, and Francesco Stellacci. Surface-structure-regulated cell-membrane penetration by monolayer-protected nanoparticles. *Nature Materials*, 7(7):588–595, jul 2008.

[10] Ayush Verma and Francesco Stellacci. Effect of Surface Properties on Nanoparticle-Cell Interactions. *Small*, 6(1):12–21, jan 2010.

[11] Reid C. Van Lehn and Alfredo Alexander-Katz. Penetration of lipid bilayers by nanoparticles with environmentally-responsive surfaces: simulations and theory. *Soft Matter*, 7(24):11392, 2011.

[12] Federica Simonelli, Davide Bochicchio, Riccardo Ferrando, and Giulia Rossi. Monolayer-Protected Anionic Au Nanoparticles Walk into Lipid Membranes Step by Step. *The Journal of Physical Chemistry Letters*, 6(16):3175–3179, aug 2015.

[13] Renato Bonomi, Francesco Selvestrel, Valentina Lombardo, Claudia Sissi, Stefano Polizzi, Fabrizio Mancin, Umberto Tonellato, and Paolo Scrimin. Phosphate Diester and DNA Hydrolysis by a Multivalent, Nanoparticle-Based Catalyst. *Journal of the American Chemical Society*, 130(47):15744–15745, nov 2008.

[14] Grégory Pieters and Leonard J. Prins. Catalytic self-assembled monolayers on gold nanoparticles. *New Journal of Chemistry*, 36(10):1931, 2012.

[15] Sharon C Glotzer and Michael J Solomon. Anisotropy of building blocks and their assembly into complex structures. *Nature Materials*, 6(7):557–562, aug 2007.

[16] S. Lin, M. Li, E. Dujardin, C. Girard, and S. Mann. One-Dimensional Plasmon Coupling by Facile Self-Assembly of Gold Nanoparticles into Branched Chain Networks. *Advanced Materials*, 17(21):2553–2559, nov 2005.

[17] Sharon C. Glotzer. Self-Assembly of Patchy Particles. *Nano Letters*, 4(8):1407–1413, aug 2004.

[18] Manigandan Sabapathy, Remya Ann Mathews K, and Ethayaraja Mani. Self-Assembly of Inverse Patchy Colloids with Tunable Patch Coverage. *Phys. Chem. Chem. Phys.*, 00:1–3, 2017.

[19] J Christopher Love, Lara a Estroff, Jennah K Kriebel, Ralph G Nuzzo, and George M Whitesides. *Self-assembled monolayers of thiolates on metals as a form of nanotechnology.*, volume 105. apr 2005.

[20] Zachary Farrell, Cameron Shelton, Caroline Dunn, and David Green. Straightforward, one-step synthesis of alkanethiol-capped silver nanoparticles from an aggregative model of growth. *Langmuir : the ACS journal of surfaces and colloids*, 29(30):9291–300, jul 2013.

[21] Chetana Singh, Alicia M Jackson, Francesco Stellacci, and Sharon C Glotzer. Exploiting substrate stress to modify nanoscale SAM patterns. *Journal of the American Chemical Society*, 131(45):16377–9, nov 2009.

[22] Pradip Kr. Ghorai and Sharon C. Glotzer. Atomistic Simulation Study of Striped Phase Separation in Mixed-Ligand Self-Assembled Monolayer Coated Nanoparticles. *The Journal of Physical Chemistry C*, 114(45):19182–19187, nov 2010.

[23] Aaron Santos, Jaime Andres Millan, and Sharon C. Glotzer. Facetted patchy particles through entropy-driven patterning of mixed ligand SAMS. *Nanoscale*, 4(8):2640, dec 2012.

[24] S. A. Egorov. Microphase separation of mixed polymer brushes physisorbed on cylindrical surfaces. *Soft Matter*, 8(14):3971, 2012.

[25] Xin Ma, Yingzi Yang, Lei Zhu, Bin Zhao, Ping Tang, and Feng Qiu. Binary mixed homopolymer brushes grafted on nanorod particles: a self-consistent field theory study. *The Journal of chemical physics*, 139(21):214902, dec 2013.

[26] Pablo Casuso, Pedro Carrasco, Iraida Loinaz, Germán Cabañero, Hans J. Grande, and Ibon Odriozola. Argentophilic hydrogels: elucidating the structure of neutral versus acidic systems. *Soft Matter*, 7(7):3627, 2011.

[27] J. M. H. M. Scheutjens and G. J. Fleer. Statistical theory of the adsorption of interacting chain molecules. 1. Partition function, segment density distribution, and adsorption isotherms. *The Journal of Physical Chemistry*, 83(12):1619–1635, jun 1979.

[28] Alexander Janz, Angela Köckritz, Lide Yao, and Andreas Martin. Fundamental calculations on the surface area determination of supported gold nanoparticles by alkanethiol adsorption. *Langmuir : the ACS journal of surfaces and colloids*, 26(9):6783–9, may 2010.

[29] PG De Gennes. *Scaling Concepts in Polymer Physics*. Cornell University Press, Ithaca, 1979.

[30] J.A. Ascencio, C. Gutiérrez-Wing, M.E. Espinosa, M. Marín, S. Tehuacanero, C. Zorrilla, and M. José-Yacamán. Structure determination of small particles by HREM imaging: theory and experiment. *Surface Science*, 396(1-3):349–368, jan 1998.

[31] Sergei A. Egorov, Hsiao-Ping Hsu, Andrey Milchev, and Kurt Binder. Semiflexible polymer brushes and the brush-mushroom crossover. *Soft Matter*, 11(13):2604–2616, 2015.

[32] Maureen B. Tracy, Haijian Chen, Dennis M. Weaver, Dariya I. Malyarenko, Maciek Sasinowski, Lisa H. Cazares, Richard R. Drake, O. John Semmes, Eugene R. Tracy, and William E. Cooke. Precision enhancement of MALDI-TOF MS using high resolution peak detection and label-free alignment. *PROTEOMICS*, 8(8):1530–1538, apr 2008.

[33] Kellen M. Harkness, Andrzej Balinski, John A. McLean, and David E. Cliffel. Nanoscale Phase Segregation of Mixed Thiolates on Gold Nanoparticles. *Angewandte Chemie International Edition*, 50(45):10554–10559, nov 2011.

[34] Chetana Singh, Pradip K. Ghorai, Mark A. Horsch, Alicia M. Jackson, Ronald G. Larson, Francesco Stellacci, and Sharon C. Glotzer. Entropy-Mediated Patterning of Surfactant-Coated Nanoparticles and Surfaces. *Physical Review Letters*, 99(22):226106, nov 2007.

[35] Henrik Grönbeck, Michael Walter, and Hannu Häkkinen. Theoretical Characterization of Cyclic Thiolated Gold Clusters. *Journal of the American Chemical Society*, 128(31):10268–10275, aug 2006.

[36] Ward Brullot, Rik Strobbe, Maud Bynens, Maarten Bloemen, Pieter-Jan Demeyer, Willem Vanderlinden, Steven De Feyter, Ventsislav K. Valev, and Thierry Verbiest. Layer-by-Layer synthesis and tunable optical properties of hybrid magneticplasmonic nanocomposites using short bifunctional molecular linkers. *Materials Letters*, 118:99–102, mar 2014.

[37] Alexander Böker, Jinbo He, Todd Emrick, and Thomas P. Russell. Self-assembly of nanoparticles at interfaces. *Soft Matter*, 3(10):1231, 2007.

[38] Zachary Farrell, Steve Merz, Jon Seager, Caroline Dunn, Sergei Egorov, and David L. Green. Development of Experiment and Theory to Detect and Predict Ligand Phase Separation on Silver Nanoparticles. *Angewandte Chemie International Edition*, 54(22):6479–6482, may 2015.

[39] Yueqiang Wang, Guang Yang, Ping Tang, Feng Qiu, Yuliang Yang, and Lei Zhu. Mixed homopolymer brushes grafted onto a nanosphere. *The Journal of chemical physics*, 134(13):134903, apr 2011.

[40] Yann Cesbron, Chris P Shaw, James P Birchall, Paul Free, and Raphaël Lévy. Stripy Nanoparticles Revisited. *Small*, 8(24):3714–3719, dec 2012.

[41] Julian Stirling, Ioannis Lekkas, Adam Sweetman, Predrag Djuranovic, Quanmin Guo, Josef Granwehr, Raphaël Lévy, and Philip Moriarty. Critical assessment of the evidence for striped nanoparticles. *PLoS ONE*, 9(11):e108482, dec 2013.

[42] Quy Khac Ong and Francesco Stellacci. Response to Critical Assessment of the Evidence for Striped Nanoparticles. *PLOS ONE*, 10(11):e0135594, nov 2015.

[43] Miao Yu and Francesco Stellacci. Response to Stripy Nanoparticles Revisited. *Small*, 8(24):3720–3726, dec 2012.

[44] Andrea Centrone, Ying Hu, Alicia M. Jackson, Giuseppe Zerbi, and Francesco Stellacci. Phase Separation on Mixed-Monolayer-Protected Metal Nanoparticles: A Study by Infrared Spectroscopy and Scanning Tunneling Microscopy. *Small*, 3(5):814–817, may 2007.

[45] Xiang Liu, Miao Yu, Hyewon Kim, Marta Mameli, and Francesco Stellacci. Determination of monolayer-protected gold nanoparticle ligandshell morphology using NMR. *Nature Communications*, 3(1):1182, jan 2012.

[46] Mauro Moglianetti, Quy Khac Ong, Javier Reguera, Kellen M. Harkness, Marta Mameli, Aurel Radulescu, Joachim Kohlbrecher, Corinne Jud, Dmitri I. Svergun, and Francesco Stellacci. Scanning tunneling microscopy and small angle neutron scattering study of mixed monolayer protected gold nanoparticles in organic solvents. *Chemical Science*, 5(3):1232, 2014.

[47] Gerd H Woehrle, Leif O Brown, and James E Hutchison. Thiol-functionalized, 1.5-nm gold nanoparticles through ligand exchange reactions: scope and mechanism of ligand exchange. *Journal of the American Chemical Society*, 127(7):2172–83, feb 2005.

[48] Carrie a. Simpson, Christopher L. Farrow, Peng Tian, Simon J L Billinge, Brian J. Huffman, Kellen M. Harkness, and David E. Cliffel. Tiopronin Gold Nanoparticle Precursor Forms Aurophilic Ring Tetramer. *Inorganic Chemistry*, 49(23):10858–10866, dec 2010.

[49] Kellen M. Harkness, Brian C. Hixson, Larissa S. Fenn, Brian N. Turner, Amanda C. Rape, Carrie a. Simpson, Brian J. Huffman, Tracy C. Okoli, John a. McLean, and David E. Cliffel. A Structural Mass Spectrometry Strategy for the Relative Quantitation of Ligands on Mixed Monolayer-Protected Gold Nanoparticles. *Analytical Chemistry*, 82(22):9268–9274, nov 2010.

[50] Kellen M. Harkness, Larissa S. Fenn, David E. Cliffel, and John a. McLean. Surface Fragmentation of Complexes from Thiolate Protected Gold Nanoparticles by Ion Mobility-Mass Spectrometry. *Analytical Chemistry*, 82(7):3061–3066, apr 2010.

[51] Chetana Singh, Ying Hu, Bishnu P Khanal, Eugene R Zubarev, Francesco Stellacci, and Sharon C Glotzer. Striped nanowires and nanorods from mixed SAMS. *Nanoscale*, 3(8):3244, 2011.

[52] Bart R Postmus, Frans a M Leermakers, and Martien a Cohen Stuart. Self-consistent field modeling of non-ionic surfactants at the silica-water interface: incorporating molecular detail. *Langmuir : the ACS journal of surfaces and colloids*, 24(8):3960–9, apr 2008.

[53] P.K. Ghorai and S.C. Glotzer. Molecular Dynamics Simulation Study of Self-Assembled Monolayers of Alkanethiol Surfactants on Spherical Gold Nanoparticles. *Journal of Physical Chemistry C*, 111(43):15857–15862, nov 2007.

[54] Quy Khac Ong, Javier Reguera, Paulo Jacob Silva, Mauro Moglianetti, Kellen Harkness, Maria Longobardi, Kunal S Mali, Christoph Renner,

Steven De Feyter, and Francesco Stellacci. High-resolution scanning tunneling microscopy characterization of mixed monolayer protected gold nanoparticles. *ACS nano*, 7(10):8529–39, oct 2013.

[55] A Dhirani, M A Hines, A J Fisher, O Ismail, and P Guyot-Sionnest. Structure of Self-Assembled Decanethiol on Ag(111): A Molecular Resolution Scanning Tunneling Microscopy Study. *Langmuir*, 11(7):2609–2614, jul 1995.

[56] Fahad Mateen, Hee-muk Oh, Wansu Jung, Micheal Binns, and Sung-kyu Hong. Metal nanoparticles based stack structured plasmonic luminescent solar concentrator. *Solar Energy*, 155:934–941, oct 2017.

[57] Matthew R. Jones, Kyle D. Osberg, Robert J. Macfarlane, Mark R. Langille, and Chad A. Mirkin. Templated Techniques for the Synthesis and Assembly of Plasmonic Nanostructures. *Chemical Reviews*, 111(6):3736–3827, jun 2011.

[58] Eiji Usukura, Shuhei Shinohara, Koichi Okamoto, Jaehoon Lim, Kookheon Char, and Kaoru Tamada. Highly confined, enhanced surface fluorescence imaging with two-dimensional silver nanoparticle sheets. *Applied Physics Letters*, 104(12):121906, mar 2014.

[59] Reid C Van Lehn, Prabhani U Atukorale, Randy P Carney, Yu-Sang Yang, Francesco Stellacci, Darrell J Irvine, and Alfredo Alexander-Katz. Effect of Particle Diameter and Surface Composition on the Spontaneous Fusion of Monolayer-Protected Gold Nanoparticles with Lipid Bilayers. *Nano Letters*, 13(9):4060–4067, sep 2013.

[60] Christopher M. Jewell, Jin-Mi Jung, Prabhani U. Atukorale, Randy P. Carney, Francesco Stellacci, and Darrell J. Irvine. Oligonucleotide Delivery by Cell-Penetrating Striped Nanoparticles. *Angewandte Chemie International Edition*, 50(51):12312–12315, dec 2011.

[61] Xuebo Quan, Chunwang Peng, Daohui Zhao, Libo Li, Jun Fan, and Jian Zhou. Molecular Understanding of the Penetration of Functionalized Gold Nanoparticles into Asymmetric Membranes. *Langmuir*, 33(1):361–371, 2017.

[62] Magdiel I. Setyawati, Chor Yong Tay, Boon Huat Bay, and David T. Leong. Gold Nanoparticles Induced Endothelial Leakiness Depends on Particle Size and Endothelial Cell Origin. *ACS Nano*, 11(5):5020–5030, may 2017.

[63] G. Laurent, C. Bernhard, S. Dufort, G. Jiménez Sánchez, R. Bazzi, F. Boschetti, M. Moreau, T. H. Vu, B. Collin, A. Oudot, N. Herath, H. Requardt, S. Laurent, L. Vander Elst, R. Muller, M. Dutreix, M. Meyer, F. Brunotte, P. Perriat, F. Lux, O. Tillement, G. Le Duc, F. Denat, and S. Roux. Minor changes in the macrocyclic ligands but

major consequences on the efficiency of gold nanoparticles designed for radiosensitization. *Nanoscale*, 8(23):12054–12065, 2016.

[64] Nirmal Goswami, Zhentao Luo, Xun Yuan, David Tai Leong, and Jianping Xie. Engineering gold-based radiosensitizers for cancer radiotherapy. *Materials Horizons*, 4(5):817–831, 2017.

[65] Eli Lechtman and Jean-Philippe Pignol. Interplay between the gold nanoparticle sub-cellular localization, size, and the photon energy for radiosensitization. *Scientific Reports*, 7(1):13268, dec 2017.

[66] Masaki Misawa and Junko Takahashi. Generation of reactive oxygen species induced by gold nanoparticles under x-ray and UV Irradiations. *Nanomedicine: Nanotechnology, Biology and Medicine*, 7(5):604–614, oct 2011.

[67] W. Melo-Bernal, V. Chernov, G. Chernov, and M. Barboza-Flores. Nanoscale dose deposition in cell structures under X-ray irradiation treatment assisted with nanoparticles: An analytical approach to the relative biological effectiveness. *Applied Radiation and Isotopes*, 138:50–55, aug 2018.

[68] OR Miranda and HT Chen. Enzyme-amplified array sensing of proteins in solution and in biofluids. *Journal of the American Chemical Society*, 132(14):5285–5289, 2010.

[69] C. Pezzato, S. Maiti, J. L.-Y. Chen, A. Cazzolaro, C. Gobbo, and L. J. Prins. Monolayer protected gold nanoparticles with metal-ion binding sites: functional systems for chemosensing applications. *Chem. Commun.*, 51(49):9922–9931, 2015.

[70] Alicia M. Jackson, Ying Hu, Paulo Jacob Silva, and Francesco Stellacci. From Homoligand- to Mixed-Ligand- Monolayer-Protected Metal Nanoparticles: A Scanning Tunneling Microscopy Investigation. *Journal of the American Chemical Society*, 128(34):11135–11149, aug 2006.

[71] Quy Ong, Zhi Luo, and Francesco Stellacci. Characterization of Ligand Shell for Mixed-Ligand Coated Gold Nanoparticles. *Accounts of Chemical Research*, 50(8):1911–1919, aug 2017.

[72] Maria ologan, Domenico Marson, Stefano Polizzi, Paolo Pengo, Silvia Boccardo, Sabrina Pricl, Paola Posocco, and Lucia Pasquato. Patchy and Janus Nanoparticles by Self-Organization of Mixtures of Fluorinated and Hydrogenated Alkanethiolates on the Surface of a Gold Core. *ACS Nano*, 10(10):9316–9325, oct 2016.

[73] Eun Seon Cho, Jiwon Kim, Baudilio Tejerina, Thomas M. Hermans, Hao Jiang, Hideyuki Nakanishi, Miao Yu, Alexander Z. Patashinski, Sharon C. Glotzer, Francesco Stellacci, and Bartosz A. Grzybowski.

Ultrasensitive detection of toxic cations through changes in the tunnelling current across films of striped nanoparticles. *Nature Materials*, 11(11):978–985, sep 2012.

[74] Rixiang Huang, Randy P Carney, Kaoru Ikuma, Francesco Stellacci, and Boris L T Lau. Effects of Surface Compositional and Structural Heterogeneity on NanoparticleProtein Interactions: Different Protein Configurations. *ACS Nano*, 8(6):5402–5412, jun 2014.

[75] Qiang-sheng Xia, Hong-ming Ding, and Yu-qiang Ma. Can dual-ligand targeting enhance cellular uptake of nanoparticles? *Nanoscale*, 9(26):8982–8989, 2017.

[76] Aliasger K. Salem, Peter C. Searson, and Kam W. Leong. Multifunctional nanorods for gene delivery. *Nature Materials*, 2(10):668–671, sep 2003.

[77] Rakesh Gupta and Beena Rai. In-silico design of nanoparticles for transdermal drug delivery application. *Nanoscale*, 10(10):4940–4951, 2018.

[78] Xiao-Dong Zhang, Zhentao Luo, Jie Chen, Shasha Song, Xun Yuan, Xiu Shen, Hao Wang, Yuanming Sun, Kai Gao, Lianfeng Zhang, Saijun Fan, David Tai Leong, Meili Guo, and Jianping Xie. Ultrasmall Glutathione-Protected Gold Nanoclusters as Next Generation Radiotherapy Sensitizers with High Tumor Uptake and High Renal Clearance. *Scientific Reports*, 5(1):8669, aug 2015.

[79] Michael C. Moulton, Laura K. Braydich-Stolle, Mallikarjuna N. Nadagouda, Samantha Kunzelman, Saber M. Hussain, and Rajender S. Varma. Synthesis, characterization and biocompatibility of green synthesized silver nanoparticles using tea polyphenols. *Nanoscale*, 2(5):763, 2010.

[80] Ellen E. Connor, Judith Mwamuka, Anand Gole, Catherine J. Murphy, and Michael D. Wyatt. Gold nanoparticles are taken up by human cells but do not cause acute cytotoxicity. *Small*, 1(3):325–327, 2005.

[81] Shuaidong Huo, Shubin Jin, Xiaowei Ma, Xiangdong Xue, Keni Yang, Anil Kumar, Paul C. Wang, Jinchao Zhang, Zhongbo Hu, and Xing-Jie Liang. Ultrasmall Gold Nanoparticles as Carriers for Nucleus-Based Gene Therapy Due to Size-Dependent Nuclear Entry. *ACS Nano*, 8(6):5852–5862, jun 2014.

[82] Jeffrey J. Kuna, Kislon Voïtchovsky, Chetana Singh, Hao Jiang, Steve Mwenifumbo, Pradip K. Ghorai, Molly M. Stevens, Sharon C. Glotzer, and Francesco Stellacci. The effect of nanometre-scale structure on interfacial energy. *Nature Materials*, 8(10):837–842, oct 2009.

[83] Santosh Kumar Meena, Claire Goldmann, Douga Nassoko, Mahamadou Seydou, Thomas Marchandier, Simona Moldovan, Ovidiu Ersen, François

Ribot, Corinne Chanéac, Clément Sanchez, David Portehault, Frederik Tielens, and Marialore Sulpizi. Nanophase Segregation of Self-Assembled Monolayers on Gold Nanoparticles. *ACS Nano*, 11(7):7371–7381, jul 2017.

[84] Alicia M Jackson, Jacob W Myerson, and Francesco Stellacci. Spontaneous assembly of subnanometre-ordered domains in the ligand shell of monolayer-protected nanoparticles. *Nature materials*, 3(5):330–6, may 2004.

[85] Yifeng Wang, Offer Zeiri, Alevtina Neyman, Francesco Stellacci, and Ira A. Weinstock. Nucleation and island growth of alkanethiolate ligand domains on gold nanoparticles. *ACS Nano*, 6(1):629–640, 2012.

[86] Zhi Luo, Domenico Marson, Quy K. Ong, Anna Loiudice, Joachim Kohlbrecher, Aurel Radulescu, Anwen Krause-Heuer, Tamim Darwish, Sandor Balog, Raffaella Buonsanti, Dmitri I. Svergun, Paola Posocco, and Francesco Stellacci. Quantitative 3D determination of self-assembled structures on nanoparticles using small angle neutron scattering. *Nature Communications*, 9(1):1343, dec 2018.

[87] Steven N. Merz, Zachary J. Farrell, Caroline J. Dunn, Richard J. Swanson, Sergei A. Egorov, and David L. Green. Theoretical and Experimental Investigation of Microphase Separation in Mixed Thiol Monolayers on Silver Nanoparticles. *ACS Nano*, 10(11):9871–9878, nov 2016.

[88] Debdip Bhandary, Vasumathi Valechi, Maria Natália D. S. Cordeiro, and Jayant K. Singh. Janus Gold Nanoparticles from Nanodroplets of Alkyl Thiols: A Molecular Dynamics Study. *Langmuir*, 33(12):3056–3067, mar 2017.

[89] V. Vasumathi and M. Natália D.S. Cordeiro. Molecular dynamics study of mixed alkanethiols covering a gold surface at three different arrangements. *Chemical Physics Letters*, 600(April):79–86, apr 2014.

[90] Vasumathi Velachi, Debdip Bhandary, Jayant K. Singh, and M. Natália D. S. Cordeiro. Structure of Mixed Self-Assembled Monolayers on Gold Nanoparticles at Three Different Arrangements. *The Journal of Physical Chemistry C*, 119(6):3199–3209, feb 2015.

[91] Zhi Luo, Jing Hou, Laure Menin, Quy Khac Ong, and Francesco Stellacci. Evolution of the Ligand Shell Morphology during Ligand Exchange Reactions on Gold Nanoparticles. *Angewandte Chemie International Edition*, 56(43):13521–13525, oct 2017.

[92] Lauren E. Marbella and Jill E. Millstone. NMR Techniques for Noble Metal Nanoparticles. *Chemistry of Materials*, 27(8):2721–2739, apr 2015.

[93] Bo Yang Yu, Caglar Elbuken, Carolyn L. Ren, and Jan P. Huissoon. Image processing and classification algorithm for yeast cell morphology in a microfluidic chip. *Journal of Biomedical Optics*, 16(6):066008, may 2011.

[94] Wheeler P. Davey. Precision Measurements of the Lattice Constants of Twelve Common Metals. *Physical Review*, 25(6):753–761, jun 1925.

[95] William L. Jorgensen. Optimized intermolecular potential functions for liquid alcohols. *The Journal of Physical Chemistry*, 90(7):1276–1284, mar 1986.

[96] Rachel Mahaffy, Reena Bhatia, and Barbara J. Garrison. Diffusion of a Butanethiolate Molecule on a Au{111} Surface. *The Journal of Physical Chemistry B*, 101(5):771–773, jan 1997.

[97] Xiongce Zhao, Yongsheng Leng, and Peter T Cummings. Self-assembly of 1,4-benzenedithiolate/tetrahydrofuran on a gold surface: a Monte Carlo simulation study. *Langmuir : the ACS journal of surfaces and colloids*, 22(9):4116–24, apr 2006.

[98] Alberto Jiménez, Antonio Sarsa, Manuel Blázquez, and Teresa Pineda. A molecular dynamics study of the surfactant surface density of alkanethiol self-assembled monolayers on gold nanoparticles as a function of the radius. *Journal of Physical Chemistry C*, 114:21309–21314, 2010.

[99] C. Vericat, M. E. Vela, G. Corthey, E. Pensa, E. Cortés, M. H. Fonticelli, F. Ibañez, G. E. Benitez, P. Carro, and R. C. Salvarezza. Self-assembled monolayers of thiolates on metals: a review article on sulfur-metal chemistry and surface structures. *RSC Advances*, 4(53):27730, 2014.

[100] Harrell Sellers, Abraham Ulman, Yitzhak Shnidman, and James E. Eilers. Structure and binding of alkanethiolates on gold and silver surfaces: implications for self-assembled monolayers. *Journal of the American Chemical Society*, 115(21):9389–9401, oct 1993.

[101] Steve Plimpton. Fast Parallel Algorithms for Short-Range Molecular Dynamics. *Journal of Computational Physics*, 117(1):1–19, mar 1995.

[102] J I Siepmann and I R Mcdonald. Domain Formation and System-Size Dependence in Simulations of Self-Assembled Monolayers. *Langmuir*, 9(17):2351–2355, 1993.

[103] Evgenii O. Fetisov and J. Ilja Siepmann. Structure and Phase Behavior of Mixed Self-Assembled Alkanethiolate Monolayers on Gold Nanoparticles: A Monte Carlo Study. *The Journal of Physical Chemistry B*, 120(8):1972–1978, mar 2016.

[104] J. Ilja Siepmann and Ian R. McDonald. Monte Carlo study of the properties of self-assembled monolayers formed by adsorption of CH 3 (CH 2) 15 SH on the (111) surface of gold. *Molecular Physics*, 79(3):457–473, jun 1993.

[105] L. Martínez, R. Andrade, E. G. Birgin, and J. M. Martínez. PACKMOL: A package for building initial configurations for molecular dynamics simulations. *Journal of Computational Chemistry*, 30(13):2157–2164, oct 2009.

[106] Jörn Ilja Siepmann and Daan Frenkel. Configurational bias Monte Carlo: a new sampling scheme for flexible chains. *Molecular Physics*, 75(1):59–70, jan 1992.

[107] J. Ilja Siepmann and Ian R. McDonald. Monte Carlo simulations of mixed monolayers. *Molecular Physics*, 75(2):255–259, 1992.

[108] Ryo Iida, Hitoshi Kawamura, Kenichi Niikura, Takashi Kimura, Shota Sekiguchi, Yasumasa Joti, Yoshitaka Bessho, Hideyuki Mitomo, Yoshinori Nishino, and Kuniharu Ijiro. Synthesis of janus-like gold nanoparticles with hydrophilic/hydrophobic faces by surface ligand exchange and their self-assemblies in water. *Langmuir*, 31(14):4054–4062, 2015.

[109] Wen Mar and Michael L. Klein. Molecular dynamics study of the self-assembled monolayer composed of S(CH2)14CH3 molecules using an all-atoms model. *Langmuir*, 10(1):188–196, jan 1994.

[110] Flavio Manea, Florence Bodar Houillon, Lucia Pasquato, and Paolo Scrimin. Nanozymes: Gold-Nanoparticle-Based Transphosphorylation Catalysts. *Angewandte Chemie International Edition*, 43(45):6165–6169, nov 2004.

[111] Paolo Pengo, Maria ologan, Lucia Pasquato, Filomena Guida, Sabrina Pacor, Alessandro Tossi, Francesco Stellacci, Domenico Marson, Silvia Boccardo, Sabrina Pricl, and Paola Posocco. Gold nanoparticles with patterned surface monolayers for nanomedicine: current perspectives. *European Biophysics Journal*, sep 2017.

[112] Quy Ong, Nikolaos Nianias, and Francesco Stellacci. A review of molecular phase separation in binary self-assembled monolayers of thiols on gold surfaces. *EPL (Europhysics Letters)*, 119(6):66001, sep 2017.

[113] Rachel S. Riley and Emily S. Day. Gold nanoparticle-mediated photothermal therapy: applications and opportunities for multimodal cancer treatment. *Wiley Interdisciplinary Reviews: Nanomedicine and Nanobiotechnology*, 9(4), 2017.

[114] Erik Edlund, Oskar Lindgren, and Martin Nilsson Jacobi. Predicting self-assembled patterns on spheres with multicomponent coatings. *Soft matter*, 10(17):2955–60, 2014.

[115] Randy P. Carney, Yann Astier, Tamara M. Carney, Kislon Voïtchovsky, Paulo H. Jacob Silva, and Francesco Stellacci. Electrical Method to Quantify Nanoparticle Interaction with Lipid Bilayers. *ACS Nano*, 7(2):932–942, feb 2013.

[116] Jason P. Koski and Amalie L. Frischknecht. Fluctuation Effects on the Brush Structure of Mixed Brush Nanoparticles in Solution. *ACS Nano*, page acsnano.7b08271, jan 2018.

[117] Xin Ma, Cangyi Chen, Yingzi Yang, and Feng Qiu. Ripple structures of mixed homopolymer brushes grafted on cylindrical surfaces: controlling the orientation of the pattern by attuning the substrate curvatures. *Soft matter*, 10(32):6005–13, aug 2014.

[118] Steven N Merz, Zachary J Farrell, Joseph Pearring, Elise Hoover, Mark Kester, Sergei A. Egorov, David L. Green, and Kateri H DuBay. Computational and Experimental Investigation of Janus-Like Monolayers on Ultrasmall Noble Metal Nanoparticles. *ACS Nano*, page acsnano.8b05188, oct 2018.

[119] Asli Raman, Carlos Jaime, and Victor F. Puntes. Domain Formation and Conformational Changes in Gold Nanoparticle Conjugates Studied Using DPD Simulations. *Langmuir*, 33(50):14502–14512, dec 2017.

[120] Kari Thorkelsson, Peter Bai, and Ting Xu. Self-assembly and applications of anisotropic nanomaterials: A review. *Nano Today*, 10(1):48–66, 2015.